



## Optimized optical design of photonic structures for transparent and opaque substrates

DELIVERABLE 3.1



This project has received funding from the European Union's Horizon 2020 research and innovation programme under grant agreement No 763989

## INFORMATION ABOUT THIS DOCUMENT

Author:	Prof. Dr. Manuel J. Mendes
Reviewer:	Prof. Dr. Hugo Águas
Participants:	UNINOVA
Work package:	3
Contractual Date of delivery to EC:	30 September 2019
Actual Date of delivery to EC:	8 October 2019
Nature:	Report
Dissemination level:	CO
Version:	1.0
Total number of pages:	26

## Table of Content

1. Introduction .....	3
2. State of the art .....	3
3. Modelling methodology .....	5
4. Results of optimized photonic-structured perovskite solar cells .....	7
4.1 Photonic-enhanced PSCs in superstrate configuration .....	8
4.2 Photonic-enhanced PSCs in substrate configuration .....	11
4.3 Angle-resolved optical response .....	14
5. Conclusions .....	15
6. References .....	17
7. Supplementary Material (SM).....	21
7.1 Materials refractive indices .....	21
7.2 Optimized Planar PSCs with superstrate configuration.....	21
7.3 Optimized Planar PSCs with substrate configuration .....	23
7.4 Angle-resolved optical response of planar PSCs .....	25
7.5 References .....	25

## 1. Introduction

The present deliverable 3.1 results from the main activities developed in Task 3.1 of APOLO project, led by UNINOVA partner. The object of this task is the computational optimization of light trapping (LT) structures, to be integrated in the Perovskite solar cells (PSCs), addressing only optical effects in the cells and neglecting, for now, electrical phenomena. Optimization algorithms implemented in an electromagnetic solver (*Lumerical FDTD*) have determined the best parameters (i.e. geometry) of the micro-structures patterned on the cells' substrate (to be latter fabricated in Task 4.3 of the project) that maximize absorption in the Perovskite layer. This allowed the determination of the generation profile ( $G$ , defined below in section 2) in the absorber and an ideal output photocurrent, which neglects electrical losses, taken as an initial figure-of-merit.

Besides determining the preferential parameters of the photonic structures, the present optimization studies have enabled the analysis of the underlying optical mechanisms (based in anti-reflection and scattering) that contribute to LT, and identify parasitic losses to be minimised in the devices. The results are here compared with theoretical analytical formalisms (e.g. Lambertian surfaces in the geometrical optics regime) for corroboration of the solutions and to gain deeper understanding of the interference-related LT mechanisms arising from the wave-optics regime. Such optical gains can be maximized by adjusting the structures' geometry; thus allowing their customization for different absorber thicknesses or distinct types of Perovskite compounds.

Here, the LT optimizations were performed for two perovskite absorber thicknesses (300 and 500 nm), to understand how to minimize the amount of absorber material while maintaining maximum light absorption. This is of great relevance to allow maximizing the cells' flexibility while keeping the 30% efficiency enhancement targeted in APOLO, relative to benchmark flexible cells without LT (KPI#4). In parallel, this will also allow reducing the amount of toxic materials to a minimum level.

## 2. State of the art

Light trapping using periodic arrays of nanostructures has proven to be an effective method to solve the well-known dichotomy where thicker solar cells are optically favorable and electrically disadvantageous, and conversely for thinner devices, ultimately opening a new window of research possibilities pointing to cost-competitive photovoltaics (PV) [1–4]. This method relies on improved anti-reflection and light scattering effects, that can be optimized to significantly enhance broadband light absorption in ultra-thin absorber layers, thereby increasing their efficiency [5,6]. This reduction in solar cells thickness also enables several advantages, be it in electronic properties such as open circuit voltage and carrier collection, or even in other properties like cells' stability and mitigation of hazardous/toxic compounds (e.g. Pb) for the case of perovskite [5,7–12]. Furthermore, it also creates a conducive scenario to improve the performance of ultra-thin and low-cost solar cells for portable electronic devices with higher intrinsic mechanical flexibility [5,6,8,13,14].

Equivalently, organic–inorganic halide perovskite semiconductors have been extensively researched during the last decade due to their impressive optoelectronic properties [5]. Perovskite solar cells (PSCs) are a promising step in the recent evolution of PV due to their high light absorption coefficient [15], tunable band structure [16,17], high charge carrier mobility [18,19], and low fabrication cost [20]. Based on the aforementioned characteristics conjoined with deeper understanding of materials and device properties, brought out by the vast research in the area of materials science, PSCs efficiency saw a rapid improvement, having grown from ~3.8% in 2009 to > 24.2% in 2019 [21–26]. However, the progress in PSC technology hitherto has been mainly achieved by optimizing the process techniques of the perovskite layer and the quality of the cells' interfaces [20,27–29].

Nevertheless, keeping a balance between generating and collecting carriers in PSCs still remains a major challenge to overcome. In conventional PSCs, a perovskite layer with typically ~500 nm thickness is required to allow sufficient light absorption (hence, photocarrier generation) and maximize efficiency. In contrast, thinner absorber layers should facilitate carrier collection at the contacts since, ideally, the perovskite thickness should

be smaller than the carrier diffusion length [30]. For instance, the carrier diffusion lengths in the commonly used methylammonium lead iodide (MAPbI<sub>3</sub>) perovskite are of about 100 nm [5,30], therefore reducing the perovskite's thickness is an important goal to minimize recombination losses. Concomitantly, the use of less amount of absorber material is also an important mean to mitigate the usage of toxic Pb [7]. However, reducing the absorber thickness comes at the expense of increasing the optical losses in PSCs; particularly for the longer sunlight wavelengths in the VIS-NIR range that require a large travel path inside the absorber to generate photocurrent. Therefore, effective light trapping (LT) strategies are crucial to improve performance in ultra-thin solar cells, ultimately enabling highly efficient and flexibility PSCs [5,6].

While silicon-based solar cells have been extensively tested regarding the implementation of advanced LT schemes, their application in PSCs is still in its infancy. This lethargy in LT adoption comes, understandably, from the high absorption properties of these perovskite materials. Regardless, for ultra-thin technology LT methodologies become viable to mitigate non-absorption losses [5,6,31]. Different LT approaches have been proposed in the last few years for PSCs, such as micro lens or nanocone arrays [32–34], random pyramids [35], fiber array-based anti-reflection front electrodes [36], nanophotonic front [37] and back electrodes [11], nanophotonic perovskite layers [7], nano- and micro-patterned charge transport layers [38,39], and corrugated substrates for single [40] and multijunction [41–43] PSCs, as well as the exploitation of surface plasmon resonances, e.g.: plasmonic nanoparticles [44–46], light grating-coupled plasmons [46] and embedding TiO<sub>2</sub> nanoparticles into the mesoporous TiO<sub>2</sub> layer [47]. Nonetheless, most of these approaches have yet to demonstrate pronounced absorption improvements that justify the efforts in their integration, or have even caused electrical deterioration of the devices.

In a previous theoretical contribution the authors presented a novel LT design, operating in the wave-optics regime [3], that was shown to allow record photocurrent gains in PSCs via the incorporation of wavelength-sized pyramidal-like features in the front electron transport layer (ETL) of cells with a substrate (*p-i-n*) configuration [5]. This enabled the demonstration of LT levels close to the ideal Lambertian limits of geometric optics. However, the implementation of such LT architecture may be difficult to realize in practice, since the photonic elements need to be patterned on top of the planar PSC layers, during the final processing stages, which may cause the degradation of the delicate materials of the cells during the micro-patterning fabrication [31,48].

In this work, we explored PSCs patterned with wave-optical semi-spheroidal LT features formed from the conformal deposition of the cells' materials onto photonic-structured substrates. Such innovative industrially-attractive LT design is studied and optimized here for two different solar cell configurations: superstrate and substrate; considering distinct perovskite absorber thicknesses (300 and 500 nm), as sketched in Fig. 1. This approach has significant practical benefits regarding its applicability, when compared with post-patterned photonic structures implemented on the ETLs, since here the PSC layers are wet-coated by usual methods over a substrate already patterned with LT structures, hence making the photonic integration independent of the PSC's fabrication. This is particularly beneficial in order to prevent the LT implementation from deteriorating not only the PSC layers but also less robust polymeric substrates used in flexible devices [13,49]. Besides, this enables the widespread application of the micro-structured substrates as generic photonic platforms to support other types of thin-film PV devices (based in Si [6], CIGS [50], CZTS [51], organic [13], tandems [52] etc.), after straightforward adaptation/tuning of the geometrical parameters of the LT structures.

Previous work has shown that hexagonal arrays of high-index semi-spheroidal features patterned on the cells' illuminated front surface allow pronounced broadband absorption enhancement in the PV absorber of thin-film solar cells [5,6,31,48]. Here, such type of features is produced in the cells' front due to the conformal deposition of the PSC layers over the patterned substrates (see Fig. 1). Apart from allowing higher optical density with thinner absorber thickness, the LT geometries investigated here provide three other practical advantages: 1) the "round" spheroidal-type shapes can avoid losses associated with nanostructures having high spatial curvatures or sharp edges [2,56]; 2) arrays of such semi-spheroidal features can be easily fabricated by industrially-attractive patterning methods such as colloidal lithography - a low cost soft-lithography process capable of engineering with nano/micrometer resolution with high uniformity throughout large areas [31,48]; 3)

the inherent wide angular acceptance of this type of structures is particularly important for flexible solar cells [6,56], since their operation under bending implies the simultaneous conversion of light coming from a broad angular range.

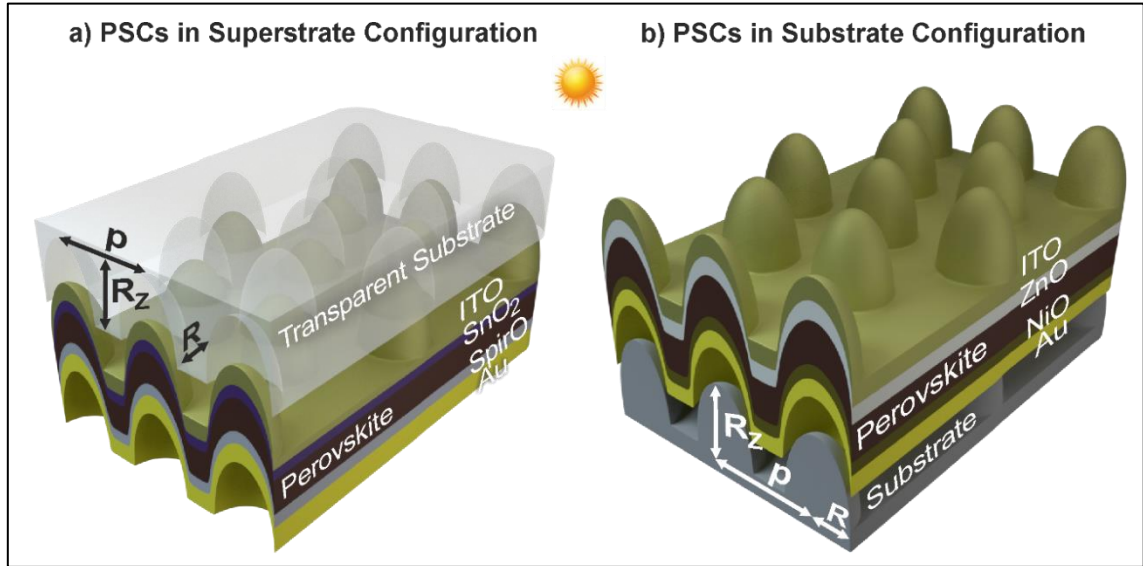


**Figure 1:** Two types of photonic-patterned substrates were studied and optimized for two types of PSC architectures: the conventional superstrate configuration (a), compatible only with transparent substrates (e.g. flexible polymers as PEN/PET) [49,53]; and the so-called “inverted” substrate configuration (b) enabling a larger variety of substrates (e.g. flexible opaque materials as metal sheets) [53–55]. The LT structures patterned on the substrates are modelled as a hexagonal array (with pitch  $p$ ) of vertically-aligned semi-prolate features with radii  $R$  and  $R_z$ , respectively along the in-plane direction and illumination axis. The PSC layers are conformally deposited over such spheroidal features: **a)** superstrate-type layer configuration, in which light comes into the devices from the substrate side, composed of transparent conducting oxide (TCO, made of ITO)/electron transport layer (ETL, made of  $\text{SnO}_2$ )/perovskite absorber (methylammonium lead iodide,  $\text{CH}_3\text{NH}_3\text{PbI}_3$ )/hole transport layer (HTL, made of Spiro-OMeTAD)/rear metal contact (made of gold, Au); **b)** substrate-type layer configuration, in which light comes into the devices from the films’ side, composed of TCO (made of ITO)/ETL (made of  $\text{ZnO}$ )/perovskite ( $\text{CH}_3\text{NH}_3\text{PbI}_3$ )/HTL (made of  $\text{NiO}_x$ )/rear contact (Au).

### 3. Modelling methodology

We employed a 3D finite difference time domain (FDTD) numerical method to rigorously model optical effects in the photonic-structured PSCs [3,5,6,57]. This method is regarded as a preferential approach for solving electromagnetic problems in the wave-optics regime, especially for light management in solar cells, mainly owing to its conceptual simplicity and versatility [3]. Furthermore, its capability for single-run broadband simulations is of particular interest for application in photovoltaics [2,5,6].

The two different PSC architectures of Fig. 1 were modelled, in which the solar cells are composed of 5 layers conformally coated onto micro-structured substrates. The optical response of the materials is determined by their complex refractive index ( $N=n+ik$ ) spectra, which were taken from published experimental data and are plotted in section S1 of Supplementary Material (SM, section 7). For the superstrate configuration (Fig. 1a), the refractive index of the transparent substrate was accounted for by a fixed real value, attributed to the background index of the simulation volume, equal to  $n=1.5$  (e.g. similar to the index of PET) [58]. For the substrate configuration (Fig. 1b), a background index  $n=1.6$  was taken in order to account for a typical transparent adhesive material used for encapsulation over the PSC layers [58].

The photonic features on the substrates are arranged in a hexagonal array, thus mimicking the structures patterned by colloidal soft-lithography [31,48]. Therefore, the FDTD computations were carried out in a 3D unit

cell, corresponding to one period of the hexagonal array [59]. The PSCs are illuminated by a plane wave source placed in the background medium above the structures. The computational unit cell was delimited by boundary conditions (BCs): perfect matching layers (PML) were applied in the top (above the source) and bottom (below the cells) planes to prevent reflections of outgoing waves, and in the lateral planes periodic BCs were set to simulate the infinite periodicity of the solar cells structure. At normal illumination, the symmetry of the LT elements relative to the incidence direction also allowed calculating only one quadrant of the unit cell, employing symmetric and anti-symmetric BCs, thus reducing the computation time [3]. However, when considering oblique illumination, for the angular study in section 4, such symmetry is broken, so periodic Bloch BCs were applied and the simulation volume was extended to the entire unit cell [6]. All the definitions of the FDTD computations (mesh geometry, number of PMLs, etc.) were carefully checked based on sets of convergence tests performed to validate the accuracy of the results.

We are interested in analyzing the light absorption along the PSC structures of Fig. 1, i.e. the power absorbed per unit volume ( $P_{ABS}$ ) in each element of the structures which is given by the resulting electric field distribution established in its material:

$$P_{ABS} = \frac{1}{2} \omega \epsilon'' |\mathbf{E}|^2 \quad (1)$$

where  $|\mathbf{E}|^2$  is the electric field intensity,  $\omega$  is the angular frequency of the light and  $\epsilon''$  is the imaginary part of the dielectric permittivity.  $P_{ABS}$  is normalized by the source power to obtain the absorption density ( $p_{ABS}$ , units of  $\text{m}^{-3}$ ). The absorption of light for a particular wavelength ( $\lambda$ ) is determined by integrating  $p_{ABS}$  along the absorber volume:  $Abs(\lambda) = \int p_{ABS}(\lambda) dV$ . The number of photons absorbed per unit volume and per unit time is the photon absorption rate:  $g(\omega) = P_{ABS}/E_{PH}$ , where  $E_{PH} = \hbar\omega$  is the photon energy. Here we consider that each absorbed photon excites one electron-hole pair, so  $g$  is equivalent to the optical generation rate. Since the illumination is provided by a broadband source, characterized by a spectral irradiance (instead of a power density), the E-field is substituted by an electric-field spectral density such that its intensity,  $|\mathbf{E}|^2$ , becomes with units of  $\text{V}^2\text{m}^{-2}\text{Hz}^{-1}$ . In this way,  $g$  is normalized to a spectral generation rate (in units of  $\text{m}^{-3}\text{s}^{-1}\text{Hz}^{-1}$ ) such that the total generation rate ( $G$ , units of  $\text{m}^{-3}\text{s}^{-1}$ ) is determined by integrating over the frequency range of the source bandwidth:  $G = \int g(\omega) d\omega$  [59].

The wavelength range of the illumination source was 300-1000 nm in all calculations, since it corresponds to the most significant portion of the photocurrent spectrum of PSCs [5]. In this study, we considered an ideal internal quantum efficiency of the PSCs equal to 100% (i.e. every photon absorbed in the perovskite material generates carriers collected by the contacts), since we are mainly concerned with the optical rather than the electrical transport behavior of the cells [3,5,6]. Thus, the photocurrent density ( $J_{PH}$ ) is determined by integrating the absorption in the perovskite material, multiplied with the solar power spectrum AM1.5G ( $I_{AM1.5}$ , units of  $\text{Wm}^{-2}\text{m}^{-1}$ ), along the chosen computation wavelength range (300-1000 nm):

$$J_{PH} = e \int \frac{\lambda}{hc} Abs(\lambda) I_{AM1.5}(\lambda) d\lambda \quad (2)$$

Where  $e$  is the electron's charge,  $h$  is Planck's constant and  $c$  is the light velocity in vacuum. This spectrally-integrated  $J_{PH}$  creates an upper-limit to the attainable short-circuit current density of the cell, since it neglects any electrical losses. Furthermore, this parameter will also be used in the simulations as the figure-of-merit to optimize the geometry of the substrate features - modelled as semi-spheroidal shapes with an axis of revolution aligned with the illumination direction.

A particle swarm optimization algorithm (PSO) [6,59] was employed in the FDTD programs to find the optimized set of parameters for the semi-spheroidal structures of the photonic substrates. Population-based stochastic optimization methods, such as PSO, are the most favorable approach to perform the complete screening of complex physical systems with a strong correlation between a high numbers of parameters, as in the present wave-optics regime, in order to determine precisely the global maximum of any given figure-of-merit. Further details concerning the PSO methodology are given in previous contributions [3,6,60].



## 4. Results of optimized photonic-structured perovskite solar cells

In this section we present the results of the optimized LT structures considering both configurations depicted in Fig. 1. The superstrate configuration (Fig. 1a) is the current record efficiency holder in PSCs [26]. Nevertheless, the requirement for superstrate solar cells to be supported on transparent substrates is a major limiting factor if one is to achieve ultra-thin and flexible devices. This can be mostly attributed to the proclivity for low degradation temperatures, usually seen in bendable transparent materials (e.g. PEN, PET), that severely restricts the PSCs fabrication conditions [53]. Subsequently, there has been a shifting interest to the substrate configuration (Fig. 1b), since it allows for a more versatile gamut of materials to be used, such as the case of opaque and much more robust bendable materials (e.g. metal foils, PI) [53–55]. Besides, the substrate-type PSC structure is compatible with its application as sub-cell in monolithic tandem devices (e.g. perovskite top cells coupled with Si [52] or CIGS [53] bottom cells), which is another research line responsible for attracting much interest lately.

The materials considered for the PSCs' layer structure are based on state-of-the-art devices produced with low-temperature ( $< 200$  °C) fabrication. Different materials are considered for the ETL and HTL in each configuration:  $\text{SnO}_2$  and  $\text{ZnO}$  are the materials taken for the ETLs, and Spiro-OMeTAD and  $\text{NiO}$  are those of the HTLs, respectively in the superstrate and substrate configuration. Apart from their low-temperature processing, both ETL materials have recently been revealing better stability and performance than the conventional  $\text{TiO}_2$  [26,61,62]. As for the HTLs, Spiro is the material that has allowed the highest efficiencies so far. However, due to its high cost, other HTLs have been investigated, being  $\text{NiO}$ -based materials those that appear to be the best alternative, especially for flexible applications that can particularly benefit from low-cost devices [63]. The conventional MAPI (methylammonium lead iodide) perovskite was taken for the absorber material, with two different thicknesses analyzed in this work: the standard 500 nm and a thinner 300 nm layer.

Table 1 shows the sets of relevant physical parameters optimized for the aforementioned cell designs, where  $R$ ,  $R_z$  and  $p$  define the geometry of the LT features patterned on the substrates (see Fig. 1) and the values  $t_{\text{layer}}$  correspond to the thickness of specific flat layers. These quantities were taken as variables by the PSO algorithm that iteratively searched for the best set of parameters that maximizes the photocurrent ( $J_{PH}$ , equation 2) produced in the perovskite material. Row 1 of Table 1 shows the *Lambertian* limits of geometrical optics for the analyzed perovskite absorber layers, as described in an earlier contribution of the authors [5]. In this case, the values of the LT enhancement were calculated relative to a cell without LT in the same regime of geometrical optics. Row 2 and 4 present the optically-optimized values for the thicknesses of the front contact of planar PSCs, which provides an anti-reflection coating (ARC) effect, and of the HTLs, respectively for superstrate and substrate configuration. These serve as reference results for comparison with the ones obtained with the photonic semi-spheroidal structures shown in rows 3 and 5, respectively. The results and discussion for the two optimized types of planar PSCs are presented in section S2 of SM (section 7).

**Table 1.** Highest  $J_{PH}$  values obtained for the optimized LT structures for two distinct PSCs, with 300 or 500 nm perovskite layer thicknesses, in two different solar cells configurations, superstrate and substrate-type, considered in this work. The geometrical optimization parameters ( $R$ ,  $R_z$ ,  $p$ ,  $t_{\text{ITO}}$ ,  $t_{\text{SnO}_2}$ ,  $t_{\text{Spiro}}$ ) and ( $R$ ,  $R_z$ ,  $p$ ,  $t_{\text{ITO}}$ ,  $t_{\text{ZnO}}$ ,  $t_{\text{NiO}}$ ), for the LT structures in superstrate and substrate configurations, respectively, are sketched in Fig. 1. The results are compared with the reference cases of planar PSCs having optically-optimized TCO/ETL and HTL thicknesses, as well as with the theoretical limits in the regime of geometrical optics attainable with a *Lambertian* scattering front surface.

Light Trapping Structures	Absorber: 300 nm Perovskite layer		Absorber: 500 nm Perovskite layer		Row index
	Optimal Parameters	$J_{PH}$ , mA/cm <sup>2</sup> (LT enhancement)	Optimal Parameters	$J_{PH}$ , mA/cm <sup>2</sup> (LT enhancement)	
<i>Lambertian</i> surface	-	<b>33.8</b> (28%)	-	<b>35.3</b> (25%)	<b>1</b>



Optimized Planar PSCs in Superstrate Configuration (Fig. S3)	$t_{ITO} = 50$ nm $t_{SnO_2} = 25$ nm $t_{Spiro} = 50$ nm <b>25.0</b>	$t_{ITO} = 50$ nm $t_{SnO_2} = 25$ nm $t_{Spiro} = 50$ nm <b>27.1</b>	<b>2</b>
Optimized Photonic PSCs in Superstrate Configuration (Fig. 2)	$t_{ITO} = 50$ nm $t_{SnO_2} = 25$ nm $t_{Spiro} = 50$ nm $R = 219.2$ nm $Rz = 167.6$ nm $p = 558.6$ nm <b>30.7</b> (22.8%)	$t_{TCO} = 50$ nm $t_{SnO_2} = 25$ nm $t_{Spiro} = 50$ nm $R = 206.2$ nm $Rz = 259.8$ nm $p = 508.1$ nm <b>32.5</b> (20.0%)	<b>3</b>
Optimized Planar PSCs in Substrate Configuration (Fig. S4)	$t_{ITO} = 50$ nm $t_{ZnO} = 100$ nm $t_{NiO} = 10$ nm <b>22.5</b>	$t_{ITO} = 50$ nm $t_{ZnO} = 100$ nm $t_{NiO} = 10$ nm <b>25.1</b>	<b>4</b>
Optimized Photonic PSCs in Substrate Configuration (Fig. 3)	$t_{ITO} = 50$ nm $t_{ZnO} = 100$ nm $t_{NiO} = 10.1$ nm $R = 239.0$ nm $Rz = 309.2$ nm $p = 480.1$ nm <b>28.0</b> (24.4%)	$t_{ITO} = 50$ nm $t_{ZnO} = 100$ nm $t_{NiO} = 11.1$ nm $R = 200.2$ nm $Rz = 519.3$ nm $p = 484.4$ nm <b>30.2</b> (20.3%)	<b>5</b>

The PSO “smart search” was constrained to certain parameters’ boundaries that were set based on reasonable values for their domains. Several optimization runs were performed with different initial parameter sets spanning the domain space, and it was found that the algorithm consistently converged to thicknesses of the contact layers ( $t_{ITO}$ ,  $t_{SnO_2}$ ,  $t_{Spiro}$ ,  $t_{ZnO}$ ,  $t_{NiO}$ ) at the minimum allowed value of the domain, defined in order to guarantee their electrical performance. Therefore, it is clear that such layers are optically undesirable, but their presence is electrically needed with a minimum thickness to guarantee effective current extraction. This aspect is further detailed in sections (S2 and S3 of SM) [3,5,6].

#### 4.1 Photonic-enhanced PSCs in superstrate configuration

We begin by analyzing the results obtained with the optimized set of geometrical parameters of PSCs in superstrate configuration (Fig. 1a), which are presented in Fig. 2. The absorption spectra of the optimized LT structures (corresponding to row 3 of Table 1) are compared to those of the planar reference cells (row 2 of Table 1) in Fig. 2a,b, for the perovskite absorber thicknesses (300 and 500 nm) considered in this study. Figs. 2c,d show the  $p_{ABS}$  profiles of PSCs with LT structures, along the xz plane passing by the center of a semi-spheroidal feature, for four different wavelengths along the illumination spectrum.

Looking at the reference planar cells (blue curves in Fig. 2a,b), both 300 and 500 nm cells show a similar broadband behavior, with the 300 nm cell showing an overall lower absorption, from the shorter light travel path in the absorber. The considerably high absorption in the perovskite active region (mainly corresponding to the 450-750 nm wavelength range in Fig. 2) evidences well the outstanding perovskite optical properties, preceded by a small absorption drop in the UV-blue range (300-450 nm) due to reflection and parasitic absorption in the front contact (ITO and  $SnO_2$  layers). This drop is slightly lower (~5%) for the 300 nm thick cell. In the near-infrared (NIR) there is a more abrupt absorption drop above 750 nm (nearing 86% and 89% for the 500 and 300 nm thickness, respectively) that coincides with the 1.5 eV bandgap of the absorber material. Regarding the photonic LT structures (red curves in Fig. 2a,b), there is a pronouncedly higher broadband absorption occurring in the perovskite, brought out by the superior light management scenario created by the photonic features, as explained below.

The results of Fig. 2 demonstrate a key optical advantage of using photonic-structured PSCs via conformal deposition over patterned substrates: the fact that it is the higher-index perovskite material that plays the main role in anti-reflection and light scattering, which causes the notable absorption gains and extremely low parasitic absorption (even lower than the reference planar cells) in most of the spectrum. The inset images of Fig. 2a,b show the cross section of the solar-spectrum-weighted generation rate ( $G$ ) along the PSCs with the optimized LT structures, computed over the 300-1000 nm wavelength range. It is notable from these inset profiles that the spectral-integrated absorption occurs primarily in the perovskite. However, Spiro-OMeTAD and Au also show some parasitic contribution, complementarily evidenced in the absorption density profiles (Fig. 2 c,d), especially for longer NIR wavelengths.

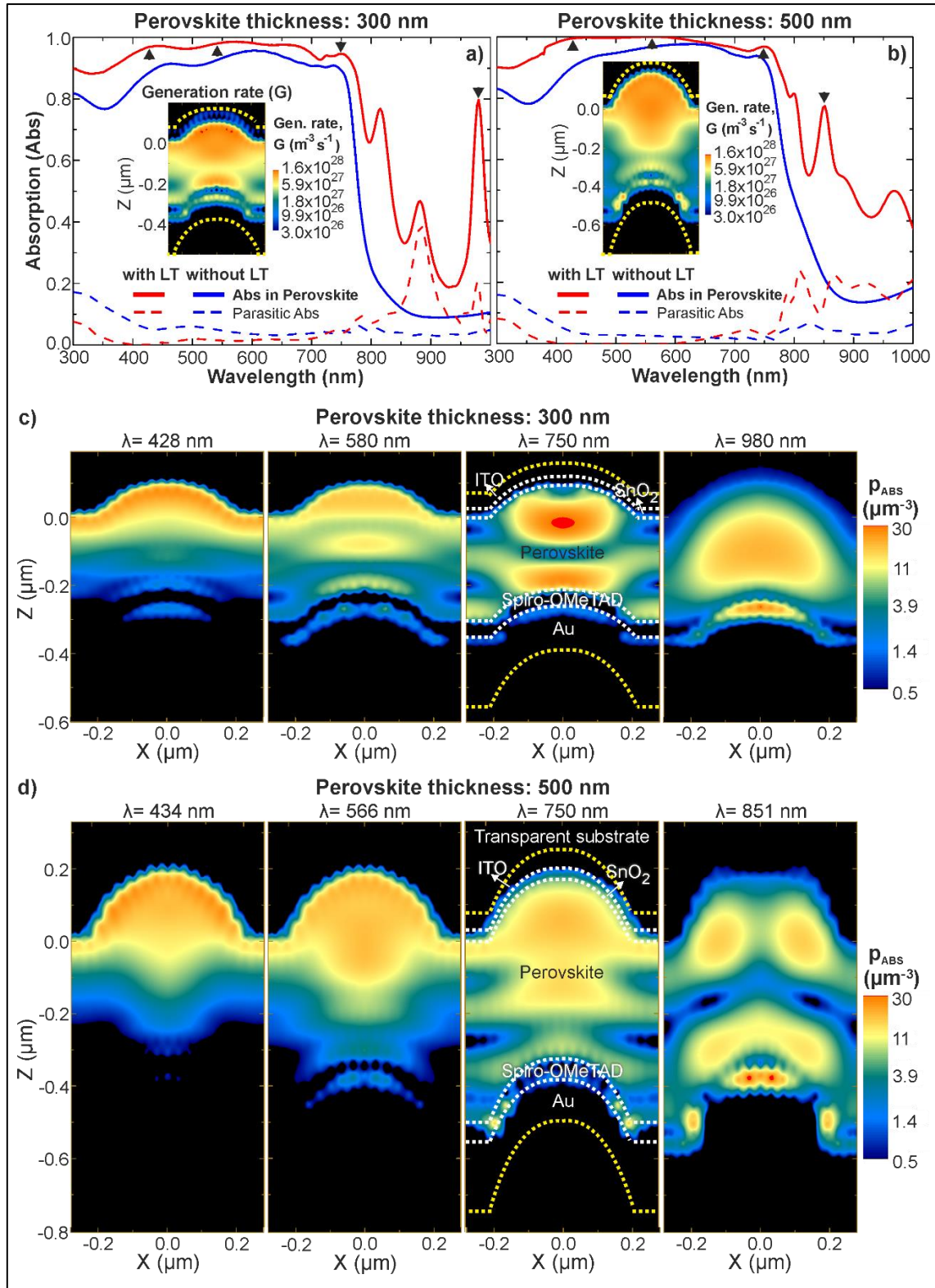


**Figure 2: a,b)** Absorption spectra obtained with the optimized LT structures sketched in Fig. 1a, for PSCs in superstrate configuration (red lines, row 3 of Table 1), compared the reference cases of optically-optimized planar cells (blue lines, row 3), for perovskite layers with distinct thickness: a) 300 nm and b) 500 nm. Each graph presents the absorption occurring in the perovskite (solid lines) and the parasitic absorption in the other materials (dashed lines). The inset profiles represent the log-scale distribution of the corresponding total generation rate,  $G$ , along the  $xz$  cross-sectional plane of the structures passing by the semi-spheroidal center. **c,d)** Log-scale distributions of the absorption density,  $p_{\text{ABS}}$ , along the same  $xz$  plane of the structures, at the wavelengths of the peaks marked by the arrows in a) and b), respectively for the PSCs with the 300 nm (c) and 500 nm (d) thick perovskite absorbers in superstrate configuration.

The absorption gains in the UV-VIS are attributed to a better light coupling towards the perovskite material by the semi-spheroidal LT features, as a consequence of two optical mechanisms: 1) superior anti-reflection owing to the geometrical index matching [5,6] caused by the curvature of the front layers (ITO, SnO<sub>2</sub> and perovskite) coupled with the propinquity amongst the real part ( $n$ ) of the refractive indices of ITO, SnO<sub>2</sub> and perovskite (plotted in the section S1 of SM). 2) Near-field forward-scattering [5,6] due to the micro-lens effect of the curvature of these three layers, which causes the focal regions of intense electric-field in the top portion of the perovskite observed in the  $G$  profiles of Fig. 2a,b and in the  $p_{ABS}$  profiles of Fig. 2c,d (mainly for the indicated wavelengths of 580 nm and 566 nm, respectively). It should be noted that the absorption enhancement observed in this spectral range (<750 nm) cannot be due to the rear contact pattern, as the light is strongly absorbed before reaching the back. In the NIR range, the remarkable absorption increase is chiefly due to the far-field forward scattering caused by the semi-spheroidal shape of both the front and rear features of the PSCs structure, which is favoured by the high real part ( $n$ ) of the perovskite refractive index. This effect manipulates the vertically-impinging light and redirects it to paths closer to the horizontal plane, thereby leading to optical path length amplification within the cell and coupling with waveguided modes. This is evidenced by the “hot-spots” observed in the  $p_{ABS}$  profiles for wavelengths >700 nm, which result from constructive interference between the light waves traveling along the incidence direction and the scattered light that travels along the plane of the cell layers suffering multiple reflections from the top and bottom surfaces of the cell. The sharp absorption peaks observed in the NIR in Fig. 2a,b are a consequence of the 3D Fabry-Perot resonances resulting from such interference.

Concerning the parasitic absorption, below 500 nm wavelengths it mainly occurs within the front ITO and SnO<sub>2</sub>, as evidenced by the  $p_{ABS}$  plots of Fig. 2c,d. For longer wavelengths it is mostly relegated to the cell's rear contact (Spiro-OMeTAD/Au), with also some contribution from SnO<sub>2</sub> as evidenced by its increasing imaginary part ( $k$ ) of the refractive index in the NIR (see Fig. S1b in SM). Again the  $p_{ABS}$  plots for >500 nm wavelengths illustrate well this effect. It should also be noted that, throughout the UV-VIS range, the photonic-structured devices show significantly lower absorption losses when compared with the reference ones. This is mostly due to the geometrical index matching caused by the front curvature of the perovskite absorber, which provides a better coupling of light towards such material with high  $n$ , preventing its back-reflection towards the ITO/SnO<sub>2</sub> top layers. Nevertheless, in the NIR range (750-1000 nm wavelengths) the parasitic absorption is notably higher with LT structures due to the plasmonic effect caused by the corrugated Au metal layer [2], as seen in the  $G$  and  $p_{ABS}$  profiles of Fig. 2, which does not occur in the flat metal present in the reference cells (see Figs. S3 and S5 of SM).

Comparing this LT design to that of additional thick photonic structures coated on top of the solar cell (as analyzed in a previous study [5], the present implementation bypasses the parasitic absorption within such thick structures, especially for shorter wavelengths. This is because of two reasons: first, the optimized thicknesses of the structured front layers of ITO (50 nm) and SnO<sub>2</sub> (25 nm) are relatively small and the same as the reference cells, thence the parasitic absorption in these materials is quite low; and second, the perovskite is the main scattering material benefiting from an extremely high absorption coefficient ( $k$  values) in this range, which also helps mitigate parasitic absorption.

## 4.2 Photonic-enhanced PSCs in substrate configuration

In this section, we analyze the results obtained with the optimized set of geometrical parameters of PSCs in substrate configuration (Fig. 1b), which are presented in Fig. 3 (corresponding to rows 4 and 5 of Table 1). The absorption profiles of Figs. 2 and 3 show a similar overall optical behavior, despite the difference in cell architecture. However, the light confinement (focusing) in the front curvatures of the perovskite is more intense for the substrate-configuration PSCs, as seen by the higher values of the generation profiles (Fig. 3a,b, insets) and of the  $p_{ABS}$  profiles (Fig. 3c,d) at the first two wavelengths, due to the more elongated shape (higher  $R_z$ ) of these optimized features relative to those of the superstrate PSCs (see Table 1), for both 300 and 500 nm absorber thicknesses. A bigger height ( $R_z$ ) is needed in the substrate configuration to provide a higher effective geometrical index matching for stronger broadband anti-reflection in the UV-VIS range, since this configuration suffers from reduced absorption throughout the 300-700 nm wavelength range, relative to the superstrate

configuration, as seen in the absorption spectra of the planar reference cells. At the same time, the structures must maintain a large scattering cross-section for path length amplification in the NIR, so the optimized lateral radii ( $R$ ) are similar in the superstrate and substrate configuration. Nonetheless, for the thinner 300 nm perovskite, stronger scattering is required to compensate for the reduced absorber thickness, which explains the larger  $R$  values of the thinner PSCs relative to the 500 nm ones. The optimal designs of the semi-spheroidal arrays converged to similar pitch ( $p$ ) for both 300 and 500 nm perovskite, with optimal  $p$  values slightly above/below 500 nm for the superstrate/substrate configuration.



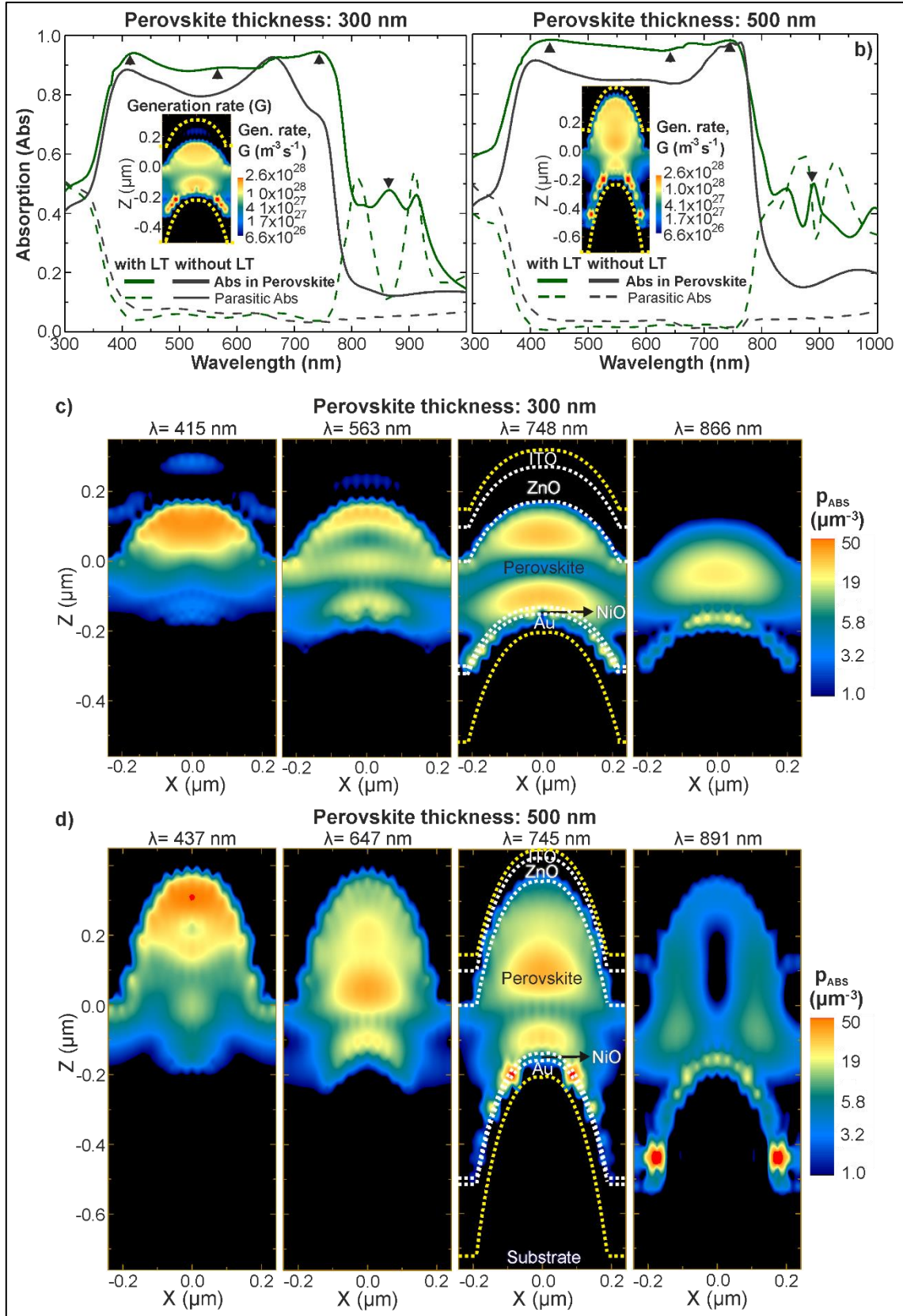


**Figure 3:** Similar to Fig. 2 but for the PSCs in substrate configuration sketched in Fig. 1b. **a,b)** Absorption spectra obtained with the optimized LT structures (green lines, row 5 of Table 1), compared with the reference cases of planar cells (grey lines, row 4), for perovskite layers with distinct thickness: a) 300 nm and b) 500 nm. The inset profiles represent the total generation rate,  $G$ , along the  $xz$  cross-sectional plane of the structures. **c,d)** Profiles of the absorption density,  $p_{\text{Abs}}$ , along the same  $xz$  plane, at the wavelengths of the peaks marked by the arrows in a) and b).



It can be seen that the substrate configuration suffers from higher parasitic absorption in most of the spectrum. At the shorter wavelengths <500 nm it is mostly attributed to the thicker 100 nm of ZnO that serves as ETL, in contrast to the 25 nm SnO<sub>2</sub> for the superstrate configuration. At the longer wavelengths in the NIR the high parasitic absorption occurs mainly at the rear contact, as revealed by the particularly intense hot spots present in the HTL and Au layers of these structures (see  $G$  and  $p_{\text{ABS}}$  profiles of Fig. 3), which exhibit a much higher magnitude than those of Fig. 2. The main reason for this is the fact that the HTL material (NiO<sub>x</sub>) considered here has a considerably higher  $n$  (see Fig. S1a of SM), so the optical optimizations converged to HTL thicknesses ( $t_{\text{NiO}} \sim 10\text{-}11$  nm) much lower than those (50 nm) taken for the Spiro-OMeTAD used in the superstrate PSCs.

Overall, the absolute photocurrent density ( $J_{\text{PH}}$ ) values attained with optimized LT are higher in the superstrate configuration, for both 300 and 500 nm perovskite, owing to the reduced parasitic absorption. However, the photocurrent improvement relative to the planar references is slightly higher in substrate configuration, mainly because the substrate-type planar cells also suffer comparably high parasitic absorption in the UV-VIS range. For this reason, the gains attainable with optimized LT designs in substrate PSCs are superior to those achieved with superstrate architecture.

### 4.3 Angle-resolved optical response

The dependence of the LT-enhanced PSCs performance with the incidence angle is of extreme relevance for their practical application, not only in conventional non-tracking PV installations, but specially importantly for thin-film cells integrated on bendable substrates [6,64]. In such case, the flexible solar cells will likely operate with a certain curvature, so they will be illuminated by a cone of incidence angles along their active area. As such, it is crucial to evaluate the LT performance for oblique illumination. Despite the fact that the LT designs described in the previous section were optimized for normal incidence, they maintain broadband light absorption enhancement for a wide range of incidence angles, as analyzed next.

At normal incidence, due to the spheroidal shape of the LT features, the optical response of the cells is independent of the polarization of the incident light, since the illumination direction is along the axis of revolution of the semi-spheroids. However, that is not the case for oblique incidence. As such, the TM (transverse magnetic) and TE (transverse electrical) polarization components were computed separately, and the resulting photocurrent densities are represented in Fig. 4d. The output photocurrent density,  $J_{\text{PH}}$ , for the unpolarized sunlight illumination was calculated by averaging the photocurrent values obtained with the TM and TE components, and is shown in Fig. 4b,c.

In general, the planar PSCs exhibit a quite omni-directional response, particularly in the substrate configuration, since the unpolarized  $J_{\text{PH}}$  (in Fig. 4b,c) is roughly constant up to  $\sim 60^\circ$  and then starts decreasing only for higher angles, as these structures do not provide scattering effects. While the unpolarized  $J_{\text{PH}}$  of the LT-enhanced PSCs generally tends to decrease with increasing angle, but the maximum reduction is only of 3-4% for the substrate configuration and of 6-7% for the superstrate configuration, for  $0\text{-}60^\circ$  incidence angles. Such small reduction mainly occurs due to the relatively lower absorption in the perovskite in the NIR range, as seen in Fig. 4d, as a consequence of slightly weaker scattering and waveguide mode coupling for larger angles. Nevertheless, such reduction with oblique incidence is significantly lower compared to that observed in thin-film silicon solar cells coated with optimized front LT structures [6]. This is attributed to the fact the present PSCs are conformally patterned on the photonic-structured substrates, so the corrugation of the PSC layers benefits a wider angular response with respect to LT-enhanced cells having a planar absorber. The more angle-independent  $J_{\text{PH}}$  of the substrate-type PSCs, relative to the superstrate configuration, is due to the fact that in substrate configuration the LT structures yield a higher fraction of absorption enhancement in the visible range (400-800 nm wavelengths) relative to NIR enhancement at longer wavelengths, and the gains in the visible (chiefly via anti-reflection) are less affected by the increase of the incidence angle as compared with those in the NIR (via scattering).

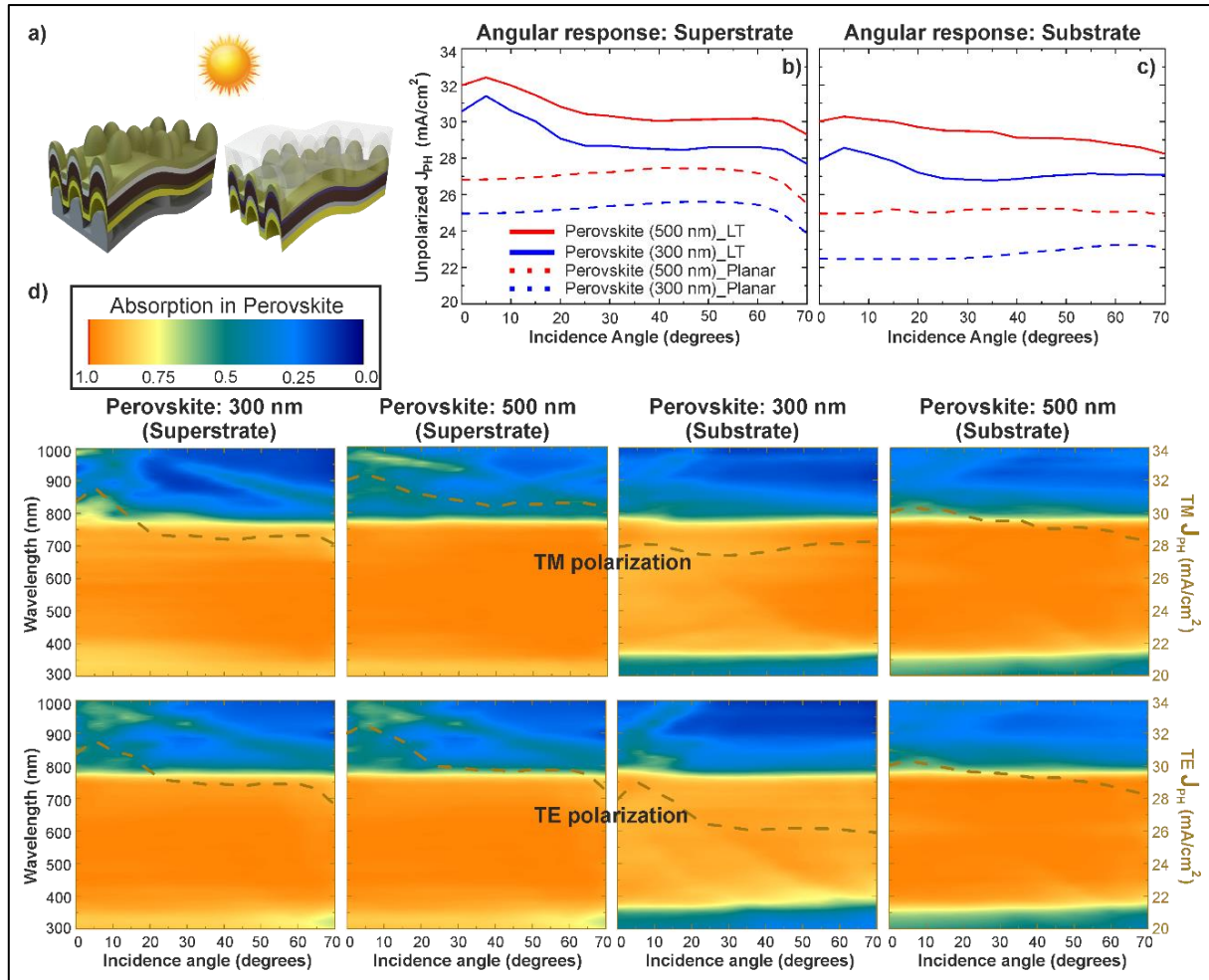


**Figure 4:** **a)** Sketch of sunlight illumination of a flexible LT-enhanced PSC. **b, c)** angle-resolved unpolarized photocurrent density,  $J_{PH}$ , given by the average between the current values attained with the TM and TE polarizations, for the two solar cells configurations: superstrate (b) and substrate (c). **d)** Color plots of the absorption spectra occurring in the 300 and 500 nm PSCs, as a function of the incidence angle, for both TM (top) and TE (bottom) polarization. The dashed brown curve plotted in the graphs corresponds to the angle-resolved photocurrent density obtained for each case (values in the right axes). See Section S4 in SM for further details regarding the angular simulations.

## 5. Conclusions

This work demonstrates the optical advantages of using photonic-structured substrates to fabricate electrically thin but optically thick solar cells, applied to perovskite PV. In the investigated light-trapping design, the active cell materials are taken to be conformally deposited over the photonic substrates. This avoids the otherwise necessary costs associated with front-textured photonics applied to the device, as well as the deterioration of the cell layers during the implementation of such LT structures. Furthermore, the present LT solution can be an extremely cost effective approach due to the low material usage, compared to those reported in the literature [5,65], as well as being compatible with industrially-attractive processes as soft-lithography and roll-to-roll [48].

By maximizing the broadband anti-reflection and light scattering properties of the devices, optimized PSC architectures were presented with unprecedented optical gains across the 300-1000 nm wavelength range of interest. To accommodate state-of-the-art fabrication procedures for these solar cells, different ETL and HTL materials were considered in the superstrate and substrate configurations [49]. Here, it is notable the resulting small thickness of the optimized ETL, HTL and TCO layers, since the optical (film-based) index-matching provides a smaller optical impact than the geometrical index-matching, thence creating a situation where smaller parasitic absorption is preferred.

The bar graph in Fig. 5 summarizes the predicted enhancements for the two distinct perovskite thicknesses of 300 and 500 nm with superstrate and substrate cells' configurations, calculated relative to the corresponding optimized planar PSC reference cases. The gains are compared with those analytically obtained in the Lambertian cases of geometrical optics (see Table 1). It should be noted that the Lambertian improvements were not calculated with respect to the same reference values of the planar PSCs, but instead relative to the same theoretical structure but without light scattering [3,5,6].

The superstrate configuration led to a higher absolute photocurrent for both perovskite thicknesses, mainly due to the thinner ETL thickness used in such architecture which yields lower parasitic absorption. Nevertheless, the substrate configuration ultimately showed ~3-4% higher gains when compared with the corresponding planar counterpart. As expected, the highest absolute photocurrents,  $J_{PH}$ , are achieved with the 500 nm thick perovskite (32.5 and 30.2 mA/cm<sup>2</sup>, respectively in superstrate and substrate configuration). However, the LT structures on the 300 nm perovskite yield the highest photocurrent improvements (~3-4% higher gains compared to those with 500 nm perovskite), as shown in Fig. 5. This matches the trend predicted from Lambertian ray optics analysis [5] - the thinner the absorber the higher the absorption enhancement that can be achieved with LT. As indicated by the dashed lines in Fig. 5a, the photocurrent gains attained with our optimized LT structures are close to those predicted by the Lambertian limits. Nevertheless, the slight differences indicate that there is still some room for further improvement of the LT scheme, for instance by tuning the refractive indices of the front (e.g. less absorbing TCO) and rear (e.g. more reflective electrode as Ag) contact layers [2,5,56].

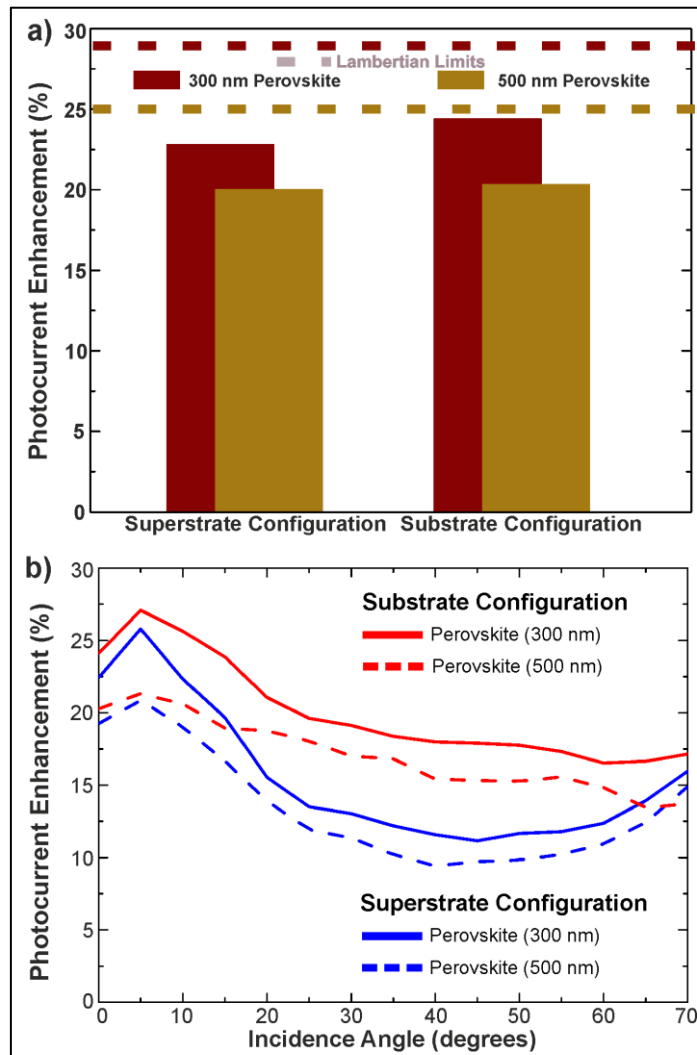


**Figure 5: a)** Improvement in photocurrent density,  $J_{PH}$ , achieved with the optimized photonic-structured PSCs (rows of 3 and 5 of Table 1) analyzed in section 3, relative to the planar references (rows 2 and 4 of Table 1 and Section S2 of SM). The Lambertian limits of LT in PSCs, in the geometrical optics regime, are also indicated by the dashed lines for the 300 and 500 nm perovskite absorbers. **b)** Angular dependence of the  $J_{PH}$  for the 4 cases in a) studied in this work.

The substantial broadband absorption enhancement provided by the LT structures, relative to planar cells, was also demonstrated for a large range of incidence angles (0-70 degrees), as summarized in Fig. 5b. The gains in the substrate configuration are clearly higher than those attained in superstrate configuration for the most part of the angular range, due to the spectral differences in which the absorption enhancements occur, as explained in section 4. It is noteworthy that the angular trends appear to be almost independent of the absorber thickness, since there is a roughly constant shift between the solid and dashed curves of Fig. 5b for the 300 and 500 nm perovskites. For both absorber thicknesses and cell configurations the angular dependences of the photocurrent improvements are significantly higher compared to those obtained in silicon solar cells with the best-performing LT front structures [6]. This is mainly due to two reasons: first, the optimized curvature of the PSC layers in the architectures analyzed in this work in which the cell is conformally coated onto structured substrates; and second, the lower real part of the refractive index (see Fig. S1 in SM) of the perovskite absorber ( $n \sim 2.3$ - $2.5$ ) and its better index matching with the contact layers ( $n \sim 1.6$ - $2.0$ ) relatively to silicon-based absorbers ( $n \sim 4$ ), which reduces parasitic absorption and reflected light escaping the cell [3,6,66]. Therefore, the optimized conformal design demonstrated in this work is preferable for flexible PSCs, as it assists their operating under higher bending angles which implies illumination coming from a broader angular range.

In addition to the superior photocurrent (thus efficiency) improvements, the LT solutions presented here reveal that the perovskite thickness can be substantially reduced while maintaining high performance, as the  $J_{PH}$  values attained with the 300 nm LT-enhanced cells are considerably higher than those of the conventional 500 nm planar references (see Table 1). Such reduction in perovskite thickness from 500 to 300 nm can bring important competitive advantages: 1) an almost 2-fold reduction in the amount of the environmentally-toxic lead (Pb) compound, as well as in the material costs associated to the perovskite material (with no additional material costs for the LT structures since they are incorporated in the substrates); 2) a potential 3-fold increase in the device flexibility due to the reduced absorber thickness.

## 6. References

- [1] H.A. Atwater, A. Polman, Plasmonics for improved photovoltaic devices, *Nat. Mater.* 9 (2010) 205–213. doi:10.1038/nmat2629.
- [2] V.E. Ferry, A. Polman, H.A. Atwater, Modeling Light Trapping in Nanostructured Solar Cells, *ACS Nano*. 5 (2011) 10055–10064. doi:10.1021/nn203906t.
- [3] M.J. Mendes, A. Araújo, A. Vicente, H. Águas, I. Ferreira, E. Fortunato, R. Martins, Design of optimized wave-optical spheroidal nanostructures for photonic-enhanced solar cells, *Nano Energy*. 26 (2016) 286–296. doi:10.1016/J.NANOEN.2016.05.038.
- [4] M.L. Brongersma, Y. Cui, S. Fan, Light management for photovoltaics using high-index nanostructures, *Nat. Mater.* 13 (2014) 451–460. doi:10.1038/nmat3921.
- [5] S. Haque, M.J. Mendes, O. Sanchez-Sobrado, H. Águas, E. Fortunato, R. Martins, Photonic-structured TiO<sub>2</sub> for high-efficiency, flexible and stable Perovskite solar cells, *Nano Energy*. 59 (2019) 91–101. doi:10.1016/J.NANOEN.2019.02.023.
- [6] M.J. Mendes, S. Haque, O. Sanchez-Sobrado, A. Araújo, H. Águas, E. Fortunato, R. Martins, Optimal-Enhanced Solar Cell Ultra-thinning with Broadband Nanophotonic Light Capture, *IScience*. 3 (2018) 238–254. doi:10.1016/j.isci.2018.04.018.
- [7] R. Schmager, G. Gomard, B.S. Richards, U.W. Paetzold, Nanophotonic perovskite layers for enhanced current generation and mitigation of lead in perovskite solar cells, *Sol. Energy Mater. Sol. Cells*. 192 (2019) 65–71. doi:10.1016/J.SOLMAT.2018.12.012.
- [8] A. V. Shah, H. Schade, M. Vanecek, J. Meier, E. Vallat-Sauvain, N. Wyrsch, U. Kroll, C. Droz, J. Bailat, Thin-film silicon solar cell technology, *Prog. Photovoltaics Res. Appl.* 12 (2004) 113–142. doi:10.1002/pip.533.

- [9] D.L. Staebler, C.R. Wronski, Reversible conductivity changes in discharge-produced amorphous Si, *Appl. Phys. Lett.* 31 (1977) 292–294. doi:10.1063/1.89674.
- [10] Y. Xu, T. Gong, J.N. Munday, The generalized Shockley-Queisser limit for nanostructured solar cells., *Sci. Rep.* 5 (2015) 13536. doi:10.1038/srep13536.
- [11] J. Wei, R.-P. Xu, Y.-Q. Li, C. Li, J.-D. Chen, X.-D. Zhao, Z.-Z. Xie, C.-S. Lee, W.-J. Zhang, J.-X. Tang, Enhanced Light Harvesting in Perovskite Solar Cells by a Bioinspired Nanostructured Back Electrode, *Adv. Energy Mater.* 7 (2017) 1700492. doi:10.1002/aenm.201700492.
- [12] M. Alexandre, M. Chapa, S. Haque, M.J. Mendes, H. Águas, E. Fortunato, R. Martins, Optimum Luminescent Down-Shifting Properties for High Efficiency and Stable Perovskite Solar Cells, *ACS Appl. Energy Mater.* 2 (2019) 2930–2938. doi:10.1021/acsaem.9b00271.
- [13] A. T. Vicente, A. Araújo, M.J. Mendes, D. Nunes, M.J. Oliveira, O. Sanchez-Sobrado, M.P. Ferreira, H. Águas, E. Fortunato, R. Martins, Multifunctional cellulose-paper for light harvesting and smart sensing applications, *J. Mater. Chem. C* 6 (2018) 3143–3181. doi:10.1039/C7TC05271E.
- [14] H. Águas, T. Mateus, A. Vicente, D. Gaspar, M.J. Mendes, W.A. Schmidt, L. Pereira, E. Fortunato, R. Martins, Thin Film Silicon Photovoltaic Cells on Paper for Flexible Indoor Applications, *Adv. Funct. Mater.* 25 (2015) 3592–3598. doi:10.1002/adfm.201500636.
- [15] Q. Chen, N. De Marco, Y. (Michael) Yang, T.-B. Song, C.-C. Chen, H. Zhao, Z. Hong, H. Zhou, Y. Yang, Under the spotlight: The organic–inorganic hybrid halide perovskite for optoelectronic applications, *Nano Today* 10 (2015) 355–396. doi:10.1016/J.NANTOD.2015.04.009.
- [16] Y. Ogomi, A. Morita, S. Tsukamoto, T. Saitho, N. Fujikawa, Q. Shen, T. Toyoda, K. Yoshino, S.S. Pandey, T. Ma, S. Hayase, CH<sub>3</sub>NH<sub>3</sub>Sn<sub>x</sub>Pb<sub>(1-x)</sub>I<sub>3</sub> Perovskite Solar Cells Covering up to 1060 nm, *J. Phys. Chem. Lett.* 5 (2014) 1004–1011. doi:10.1021/jz5002117.
- [17] J.H. Noh, S.H. Im, J.H. Heo, T.N. Mandal, S. Il Seok, Chemical Management for Colorful, Efficient, and Stable Inorganic–Organic Hybrid Nanostructured Solar Cells, *Nano Lett.* 13 (2013) 1764–1769. doi:10.1021/nl400349b.
- [18] C.S. Ponseca, T.J. Savenije, M. Abdellah, K. Zheng, A. Yartsev, T. Pascher, T. Harlang, P. Chabera, T. Pullerits, A. Stepanov, J.-P. Wolf, V. Sundström, Organometal Halide Perovskite Solar Cell Materials Rationalized: Ultrafast Charge Generation, High and Microsecond-Long Balanced Mobilities, and Slow Recombination, *J. Am. Chem. Soc.* 136 (2014) 5189–5192. doi:10.1021/ja412583t.
- [19] H. Oga, A. Saeki, Y. Ogomi, S. Hayase, S. Seki, Improved Understanding of the Electronic and Energetic Landscapes of Perovskite Solar Cells: High Local Charge Carrier Mobility, Reduced Recombination, and Extremely Shallow Traps, *J. Am. Chem. Soc.* 136 (2014) 13818–13825. doi:10.1021/ja506936f.
- [20] F. Huang, M. Li, P. Siffalovic, G. Cao, J. Tian, From scalable solution fabrication of perovskite films towards commercialization of solar cells, *Energy Environ. Sci.* 12 (2019) 518–549. doi:10.1039/C8EE03025A.
- [21] A. Kojima, K. Teshima, Y. Shirai, T. Miyasaka, Organometal Halide Perovskites as Visible-Light Sensitizers for Photovoltaic Cells, *J. Am. Chem. Soc.* 131 (2009) 6050–6051. doi:10.1021/ja809598r.
- [22] M. Saliba, T. Matsui, J.-Y. Seo, K. Domanski, J.-P. Correa-Baena, M.K. Nazeeruddin, S.M. Zakeeruddin, W. Tress, A. Abate, A. Hagfeldt, M. Grätzel, Cesium-containing triple cation perovskite solar cells: improved stability, reproducibility and high efficiency, *Energy Environ. Sci.* 9 (2016) 1989–1997. doi:10.1039/C5EE03874J.
- [23] D. Bi, C. Yi, J. Luo, J.-D. Décoppet, F. Zhang, S.M. Zakeeruddin, X. Li, A. Hagfeldt, M. Grätzel, Polymer-templated nucleation and crystal growth of perovskite films for solar cells with efficiency greater than 21%, *Nat. Energy* 1 (2016) 16142. doi:10.1038/nenergy.2016.142.
- [24] W.S. Yang, B.-W. Park, E.H. Jung, N.J. Jeon, Y.C. Kim, D.U. Lee, S.S. Shin, J. Seo, E.K. Kim, J.H. Noh, S. Il Seok, Iodide management in formamidinium-lead-halide-based perovskite layers for efficient solar cells., *Science* 356 (2017) 1376–1379. doi:10.1126/science.aan2301.
- [25] Y. Cheng, F. So, S.-W. Tsang, Progress in air-processed perovskite solar cells: from crystallization to photovoltaic performance, *Mater. Horizons* (2019). doi:10.1039/C9MH00325H.
- [26] Best Research-Cell Efficiency Chart | Photovoltaic Research | NREL, (n.d.). <https://www.nrel.gov/pv/cell-efficiency.html> (accessed September 9, 2019).
- [27] J. Burschka, N. Pellet, S.-J. Moon, R. Humphry-Baker, P. Gao, M.K. Nazeeruddin, M. Grätzel, Sequential deposition as a route to high-performance perovskite-sensitized solar cells, *Nature* 499 (2013) 316–319. doi:10.1038/nature12340.



- [28] W. Nie, H. Tsai, R. Asadpour, J.-C. Blancon, A.J. Neukirch, G. Gupta, J.J. Crochet, M. Chhowalla, S. Tretiak, M.A. Alam, H.-L. Wang, A.D. Mohite, High-efficiency solution-processed perovskite solar cells with millimeter-scale grains, *Science* (80-. ). 347 (2015) 522–525. doi:10.1126/SCIENCE.AAA0472.
- [29] N. Arora, M.I. Dar, A. Hinderhofer, N. Pellet, F. Schreiber, S.M. Zakeeruddin, M. Grätzel, Perovskite solar cells with CuSCN hole extraction layers yield stabilized efficiencies greater than 20%, *Science* (80-. ). 358 (2017) 768–771. doi:10.1126/SCIENCE.AAM5655.
- [30] T.M. Brenner, D.A. Egger, L. Kronik, G. Hodes, D. Cahen, Hybrid organic–inorganic perovskites: low-cost semiconductors with intriguing charge-transport properties, *Nat. Rev. Mater.* 1 (2016) 15007. doi:10.1038/natrevmats.2015.7.
- [31] O. Sanchez-Sobrado, M.J. Mendes, S. Haque, T. Mateus, H. Aguas, E. Fortunato, R. Martins, Lightwave trapping in thin film solar cells with improved photonic-structured front contacts, *J. Mater. Chem. C* 7 (2019) 6456–6464. doi:10.1039/C8TC06092D.
- [32] A. Peer, R. Biswas, J.-M. Park, R. Shinar, J. Shinar, Light management in perovskite solar cells and organic LEDs with microlens arrays, *Opt. Express* 25 (2017) 10704. doi:10.1364/OE.25.010704.
- [33] H. Wang, B. Cai, X. Yuan, Significant light absorption improvement in perovskite/CIGS tandem solar cells with dielectric nanocone structures, *J. Phys. Conf. Ser.* 844 (2017) 012004. doi:10.1088/1742-6596/844/1/012004.
- [34] N. Horiuchi, Photonic nanojets, *Nat. Photonics* 6 (2012) 138–139. doi:10.1038/nphoton.2012.43.
- [35] B. Dudem, J.H. Heo, J.W. Leem, J.S. Yu, S.H. Im, CH<sub>3</sub>NH<sub>3</sub>PbI<sub>3</sub> planar perovskite solar cells with antireflection and self-cleaning function layers, *J. Mater. Chem. A* 4 (2016) 7573–7579. doi:10.1039/C6TA01800A.
- [36] T.K. Nguyen, P.T. Dang, K.Q. Le, Numerical design of thin perovskite solar cell with fiber array-based anti-reflection front electrode for light-trapping enhancement, *J. Opt.* 18 (2016) 125901. doi:10.1088/2040-8978/18/12/125901.
- [37] U.W. Paetzold, W. Qiu, F. Finger, J. Poortmans, D. Cheyns, Nanophotonic front electrodes for perovskite solar cells, *Appl. Phys. Lett.* 106 (2015) 173101. doi:10.1063/1.4918751.
- [38] S.M. Kang, S. Jang, J.-K. Lee, J. Yoon, D.-E. Yoo, J.-W. Lee, M. Choi, N.-G. Park, Moth-Eye TiO<sub>2</sub> Layer for Improving Light Harvesting Efficiency in Perovskite Solar Cells, *Small* 12 (2016) 2443–2449. doi:10.1002/sml.201600428.
- [39] S.-J. Ha, J.H. Heo, S.H. Im, J.H. Moon, Mesoscopic CH<sub>3</sub>NH<sub>3</sub>PbI<sub>3</sub> perovskite solar cells using TiO<sub>2</sub> inverse opal electron-conducting scaffolds, *J. Mater. Chem. A* 5 (2017) 1972–1977. doi:10.1039/C6TA07004C.
- [40] Y. Luo, S. Liu, N. Barange, L. Wang, F. So, Perovskite Solar Cells on Corrugated Substrates with Enhanced Efficiency, *Small* 12 (2016) 6346–6352. doi:10.1002/sml.201601974.
- [41] J. Werner, F. Sahli, F. Fu, J.J. Diaz Leon, A. Walter, B.A. Kamino, B. Niesen, S. Nicolay, Q. Jeangros, C. Ballif, Perovskite/Perovskite/Silicon Monolithic Triple-Junction Solar Cells with a Fully Textured Design, *ACS Energy Lett.* 3 (2018) 2052–2058. doi:10.1021/acsenergylett.8b01165.
- [42] D. Chen, P. Manley, P. Tockhorn, D. Eisenhauer, G. Köppel, M. Hammerschmidt, S. Burger, S. Albrecht, C. Becker, K. Jäger, Nanophotonic light management for perovskite–silicon tandem solar cells, *J. Photonics Energy* 8 (2018) 1. doi:10.1117/1.JPE.8.022601.
- [43] M.I. Hossain, W. Qarony, V. Jovanov, Y.H. Tsang, D. Knipp, Nanophotonic design of perovskite/silicon tandem solar cells, *J. Mater. Chem. A* 6 (2018) 3625–3633. doi:10.1039/C8TA00628H.
- [44] J. Hao, H. Hao, J. Li, L. Shi, T. Zhong, C. Zhang, J. Dong, J. Xing, H. Liu, Z. Zhang, Light Trapping Effect in Perovskite Solar Cells by the Addition of Ag Nanoparticles, Using Textured Substrates., *Nanomater. (Basel, Switzerland)* 8 (2018). doi:10.3390/nano8100815.
- [45] R.T. Ginting, S. Kaur, D.-K. Lim, J.-M. Kim, J.H. Lee, S.H. Lee, J.-W. Kang, Plasmonic Effect of Gold Nanostars in Highly Efficient Organic and Perovskite Solar Cells, *ACS Appl. Mater. Interfaces* 9 (2017) 36111–36118. doi:10.1021/acsami.7b11084.
- [46] M. Long, Z. Chen, T. Zhang, Y. Xiao, X. Zeng, J. Chen, K. Yan, J. Xu, Ultrathin efficient perovskite solar cells employing a periodic structure of a composite hole conductor for elevated plasmonic light harvesting and hole collection, *Nanoscale* 8 (2016) 6290–6299. doi:10.1039/C5NR05042A.
- [47] J. Yin, H. Qu, J. Cao, H. Tai, J. Li, N. Zheng, Light absorption enhancement by embedding submicron scattering TiO<sub>2</sub> nanoparticles in perovskite solar cells, *RSC Adv* 6 (2016) 24596–24602. doi:10.1039/C6RA01894G.
- [48] O. Sanchez-Sobrado, M.J. Mendes, S. Haque, T. Mateus, A. Araujo, H. Aguas, E. Fortunato, R. Martins, Colloidal-lithographed TiO<sub>2</sub> photonic nanostructures for solar cell light trapping, *J. Mater. Chem. C* 5 (2017) 6852–6861. doi:10.1039/C7TC01756A.



- [49] D. Yang, R. Yang, S. Priya, S.F. Liu, Recent Advances in Flexible Perovskite Solar Cells: Fabrication and Applications, *Angew. Chemie Int. Ed.* 58 (2019) 4466–4483. doi:10.1002/anie.201809781.
- [50] P.M.P. Salomé, B. Vermang, R. Ribeiro-Andrade, J.P. Teixeira, J.M. V. Cunha, M.J. Mendes, S. Haque, J. Borme, H. Águas, E. Fortunato, R. Martins, J.C. González, J.P. Leitão, P.A. Fernandes, M. Edoff, S. Sadewasser, Passivation of Interfaces in Thin Film Solar Cells: Understanding the Effects of a Nanostructured Rear Point Contact Layer, *Adv. Mater. Interfaces.* 5 (2018) 1701101. doi:10.1002/admi.201701101.
- [51] F. Neves, A. Stark, N. Schell, M.J. Mendes, H. Águas, E. Fortunato, R. Martins, J.B. Correia, A. Joyce, Investigation of single phase  $Cu_2ZnSn_{1-x}Sb_xS_4$  compounds processed by mechanochemical synthesis, *Phys. Rev. Mater.* 2 (2018) 075404. doi:10.1103/PhysRevMaterials.2.075404.
- [52] M. Chapa, M.F. Alexandre, M.J. Mendes, H. Águas, E. Fortunato, R. Martins, All-Thin-Film Perovskite/C–Si Four-Terminal Tandems: Interlayer and Intermediate Contacts Optimization, *ACS Appl. Energy Mater.* 2 (2019) 3979–3985. doi:10.1021/acsaem.9b00354.
- [53] F. Fu, T. Feurer, T.P. Weiss, S. Pisoni, E. Avancini, C. Andres, S. Buecheler, A.N. Tiwari, High-efficiency inverted semi-transparent planar perovskite solar cells in substrate configuration, *Nat. Energy.* 2 (2016) 16190. doi:10.1038/nenergy.2016.190.
- [54] L. Qiu, J. Deng, X. Lu, Z. Yang, H. Peng, Integrating Perovskite Solar Cells into a Flexible Fiber, *Angew. Chemie Int. Ed.* 53 (2014) 10425–10428. doi:10.1002/anie.201404973.
- [55] M. Jošt, S. Albrecht, L. Kegelmann, C.M. Wolff, F. Lang, B. Lipovšek, J. Krč, L. Korte, D. Neher, B. Rech, M. Topič, Efficient Light Management by Textured Nanoimprinted Layers for Perovskite Solar Cells, *ACS Photonics.* 4 (2017) 1232–1239. doi:10.1021/acsp Photonics.7b00138.
- [56] V.E. Ferry, M.A. Verschuuren, M.C. van Lare, R.E.I. Schropp, H.A. Atwater, A. Polman, Optimized Spatial Correlations for Broadband Light Trapping Nanopatterns in High Efficiency Ultrathin Film a-Si:H Solar Cells, *Nano Lett.* 11 (2011) 4239–4245. doi:10.1021/nl202226r.
- [57] M.G. Deceglie, V.E. Ferry, A.P. Alivisatos, H.A. Atwater, Design of Nanostructured Solar Cells Using Coupled Optical and Electrical Modeling, *Nano Lett.* 12 (2012) 2894–2900. doi:10.1021/nl300483y.
- [58] Refractive index database, (n.d.). <https://refractiveindex.info/> (accessed June 1, 2018).
- [59] FDTD Solutions | Lumerical's Nanophotonic FDTD Simulation Software, (n.d.). <https://www.lumerical.com/tcad-products/fdtd/> (accessed March 7, 2018).
- [60] M.J. Mendes, H.K. Schmidt, M. Pasquali, Brownian Dynamics Simulations of Single-Wall Carbon Nanotube Separation by Type Using Dielectrophoresis, *J. Phys. Chem. B.* 112 (2008) 7467–7477. doi:10.1021/jp711450w.
- [61] Q. Jiang, X. Zhang, J. You,  $SnO_2$ : A Wonderful Electron Transport Layer for Perovskite Solar Cells, *Small.* 14 (2018) 1801154. doi:10.1002/smll.201801154.
- [62] P. Zhang, J. Wu, T. Zhang, Y. Wang, D. Liu, H. Chen, L. Ji, C. Liu, W. Ahmad, Z.D. Chen, S. Li, Perovskite Solar Cells with ZnO Electron-Transporting Materials, *Adv. Mater.* 30 (2018) 1703737. doi:10.1002/adma.201703737.
- [63] A. Al Mamun, T.T. Ava, T.M. Abdel-Fattah, H.J. Jeong, M.S. Jeong, S. Han, H. Yoon, G. Namkoong, Effect of hot-casted NiO hole transport layer on the performance of perovskite solar cells, *Sol. Energy.* 188 (2019) 609–618. doi:10.1016/J.SOLENER.2019.06.040.
- [64] P. Spinelli, M.A. Verschuuren, A. Polman, Broadband omnidirectional antireflection coating based on subwavelength surface Mie resonators, *Nat. Commun.* 3 (2012) 692. doi:10.1038/ncomms1691.
- [65] H. Zhang, J. Toudert, Optical management for efficiency enhancement in hybrid organic-inorganic lead halide perovskite solar cells, *Sci. Technol. Adv. Mater.* 19 (2018) 411–424. doi:10.1080/14686996.2018.1458578.
- [66] W. Qarony, M.I. Hossain, A. Salleo, D. Knipp, Y.H. Tsang, Rough versus planar interfaces: How to maximize the short circuit current of perovskite single and tandem solar cells, *Mater. Today Energy.* 11 (2019) 106–113. doi:10.1016/J.MTENER.2018.10.001.

## 7. Supplementary Material (SM)

### 7.1 Materials refractive indices

The complex refractive indices ( $N=n+ik$ ) of the materials considered in the finite-difference time domain (FDTD) simulations performed in this work were taken from literature databases [1] and are plotted in Fig S1.

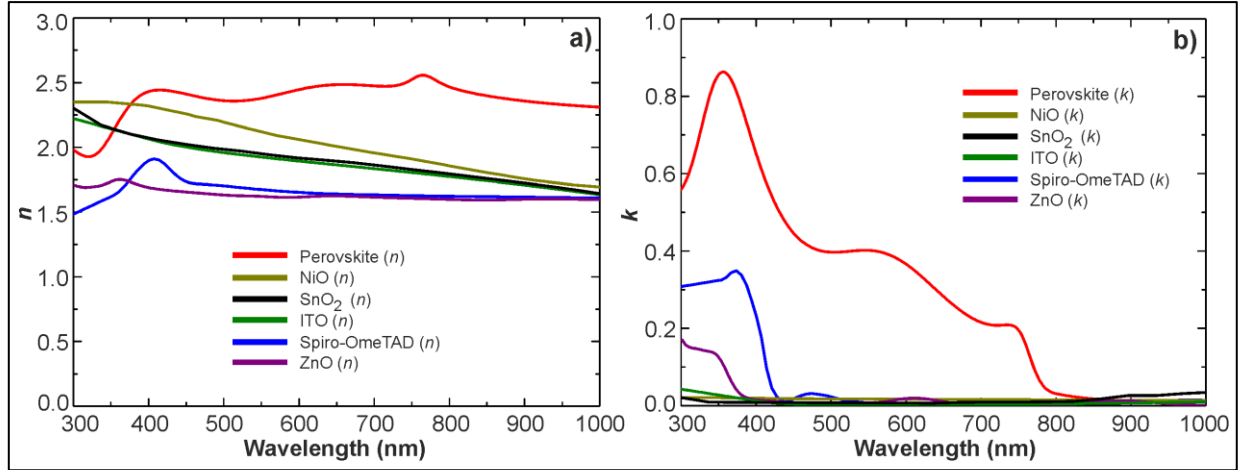


**Figure S1:** Spectra of the real,  $n$  (a), and imaginary,  $k$  (b), parts of the complex refractive indices of the materials used in this work.

### 7.2 Optimized Planar PSCs with superstrate configuration

In this section, we analyze the optical optimization of the flat layers at the front and rear contacts of the planar superstrate PSCs used as references (see Fig. 1a), i.e. the front transparent conductive oxide (TCO, made of ITO) and electron transport layer (ETL, made of  $\text{SnO}_2$ ), as well as the rear hole transport layer (HTL, made of Spiro-OMeTAD). At the cell front surface, the combined TCO and ETL can act as a planar anti-reflection coating (ARC), while at the rear the HTL and Au mirror can reflect the light of longer wavelengths back into the absorber.

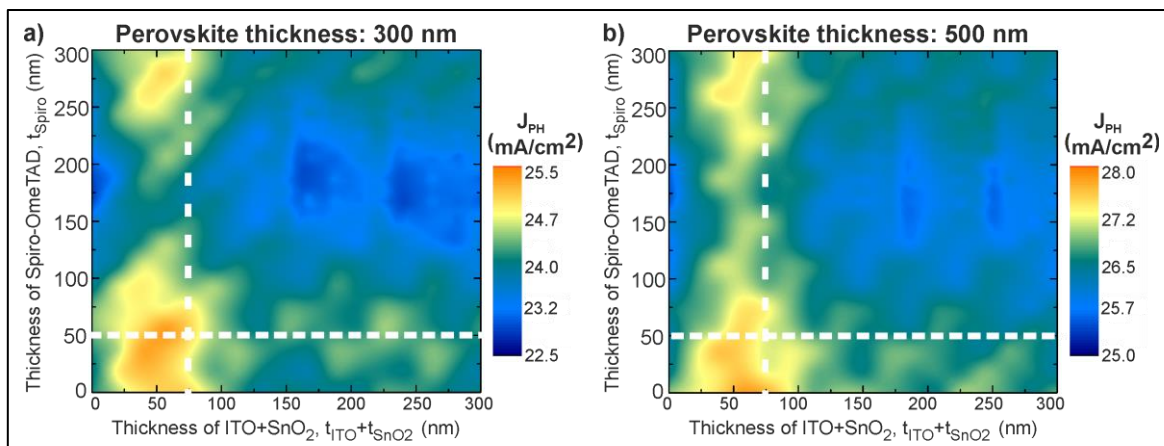


**Figure S2:** Contour plots of the calculated  $J_{PH}$  in PSCs with a planar superstrate configuration, having either a 300 nm (a) or 500 nm (b) perovskite absorber layer, as a function of the thicknesses of the front-located layers ( $t_{ITO} + t_{\text{SnO}_2}$ ) and HTL ( $t_{\text{Spiro}}$ ). The device layer structure is: flat transparent substrate/TCO (ITO)/ETL ( $\text{SnO}_2$ )/perovskite absorber/HTL (Spiro-OMeTAD)/metal electrode (200 nm Au), and light enters from the substrate side. The vertical and horizontal dashed lines mark the minimum thicknesses of the layers required to establish a good-performing selective contact, which were taken as the minimum reasonable values for these parameters:  $t_{ITO}$  (50 nm),  $t_{\text{SnO}_2}$  (25 nm) and  $t_{\text{Spiro}}$  (50 nm).

To enhance such optical properties, we carried out optimization sweeps to find the best parameters of  $t_{ITO}$ ,  $t_{SnO_2}$ , and  $t_{Spiro}$  that provide maximum photocurrent density ( $J_{PH}$ ) for the planar PSCs in superstrate configuration, in the absence of photonic structures. The high similarity between the refractive indices of ITO and  $SnO_2$  (see Fig. S1) allows simplifying the optimization procedure by optically considering these two layers as a single layer with thickness  $t_{ITO}+t_{SnO_2}$ . Therefore the maximum  $J_{PH}$  can be found by sweeping only 2 parameters, as plotted in Fig. S2. The figure shows that the highest photocurrent occurs with a combined thickness of ITO and  $SnO_2$  in the range of 20-80 nm, along with a Spiro-OmeTAD thickness below  $\sim 75$  nm, for both 300 and 500 nm thick perovskite. Nonetheless, one must also consider the electrical properties in order to select the minimum thicknesses of these layers to allow efficient selective collection of electron and hole carriers. From the electrical standpoint, it is necessary to have a minimum thickness of 50 nm for ITO, 25 nm for  $SnO_2$  and 50 nm for Spiro-OmeTAD [2–4]. As such, these were the minimum values allowed for the thicknesses of the layers (see row 2 of Table 1), and therefore the most reasonable choices when considering both optical and electrical points of view. Nevertheless, it can be seen in Fig. S2 that there is a large tolerance in the Spiro-OmeTAD thickness if the combined thicknesses of ITO and  $SnO_2$  lie within the vertical stripe of  $\sim 30$ -80 nm, particularly in the case of the 500 nm absorber.

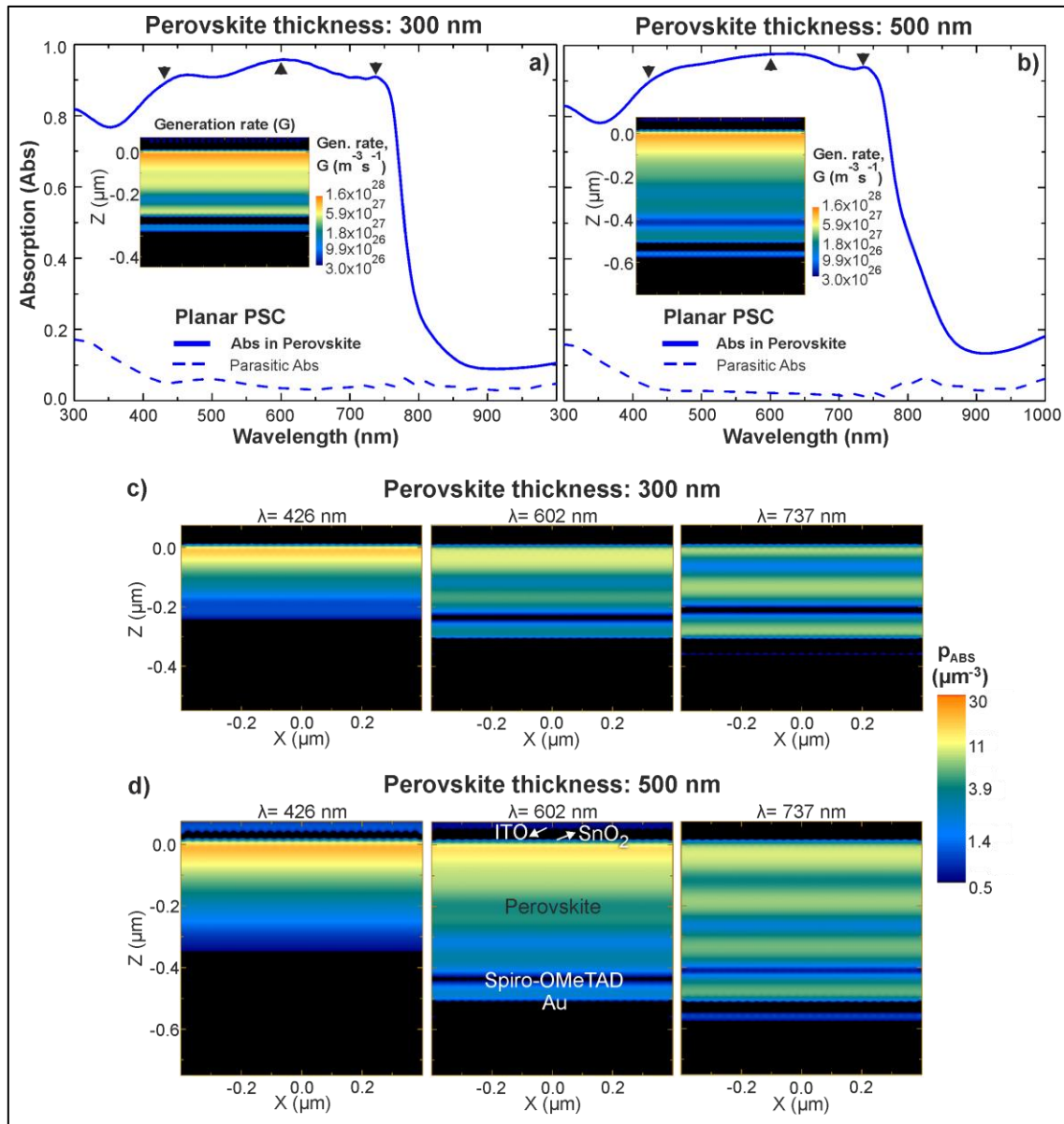


**Figure S3:** a,b) Spectra of the light absorption, obtained with the optimized thicknesses of the TCO, ETL and HTL layers indicated in Table 1 (row 2), occurring in the perovskite absorber (solid lines) and the parasitic absorption in the other

materials (dashed lines), considering perovskite films with distinct thickness: a) 300 nm and b) 500 nm, in superstrate configuration. The inset profiles show the log-scale distribution of the corresponding total generation rate,  $G$ , along the  $xz$  cross-sectional plane of the structures. The top surface of the perovskite layer is located at  $z=0$ . c,d) Log scale distributions of the absorption per unit volume ( $p_{\text{ABS}}$ ) along the same  $xz$  cross-sectional plane of the structures, at the wavelengths ( $\lambda$ ) of the absorption peaks marked by the black triangles in a) and b).

The light absorption spectra and the absorption density profiles of the planar PSCs in superstrate configuration, with the selected thicknesses of Table 1 (row 2), are shown in Fig. S3a,b and Fig. S3c,d, respectively. Since the structures are fully flat they do not provide any scattering effects, so the horizontal patterns seen in Fig. S3 are mainly caused by 1D Fabry-Perot interference of the light waves traveling back and forth along the illumination axis. The absorption occurring in both 300 and 500 nm perovskite is relatively high in the visible range, namely between 420 and 750 nm wavelengths, due to the efficient suppression of outgoing light waves caused by the optimized ARC (front layers), as well as to the high absorption coefficient of the perovskite material in this range, which is visualized by the  $p_{\text{ABS}}$  profiles of Figure S3c,d. However, the overall absorption is slightly lower (about ~8%) in such wavelength range for the 300 nm perovskite, mainly due to a reduced anti-reflection performance.

The significant absorption drop in the shorter wavelengths range of 300-400 nm is mainly caused by the parasitic absorption in the front layers, as seen in the absorption spectra of Fig. S3a,b. Moreover, above 755 nm wavelength there is a sharp drop in absorption corresponding to the bandgap of the perovskite (at ~800 nm). Therefore, it is in this NIR range, particularly for thinner perovskite layer, where the use of effective light trapping schemes can lead to the highest absorption enhancement, as investigated in this work.

### 7.3 Optimized Planar PSCs with substrate configuration

Similarly to the previous section, optical optimizations of the front (TCO, made of ITO) and rear (HTL, made of  $\text{NiO}_x$ ) contact layers were performed for the planar PSCs with a substrate configuration (see Fig. 1b). In this case, we used a fixed minimum value for thickness of the ETL (100 nm), made of ZnO, so the maximum  $J_{\text{PH}}$  was found by performing the double parameter sweeps represented in Fig. S4.

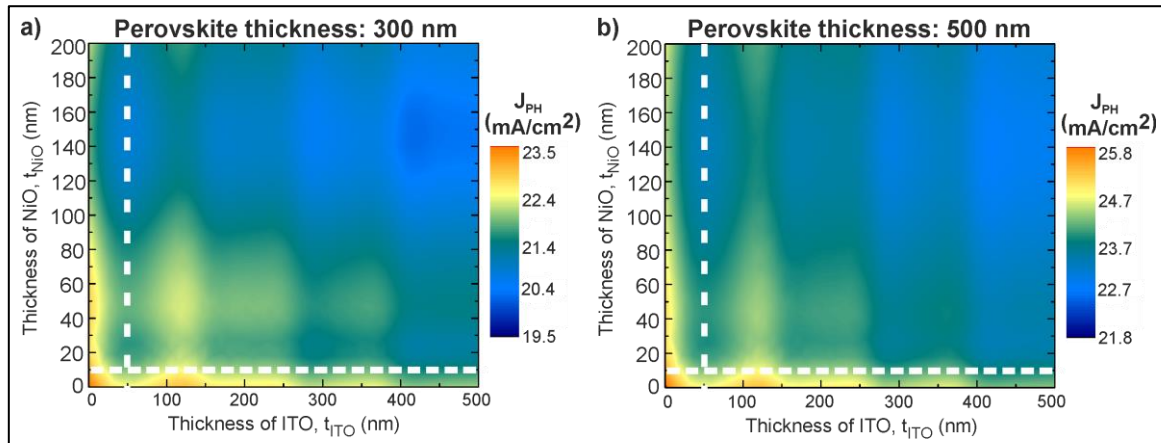
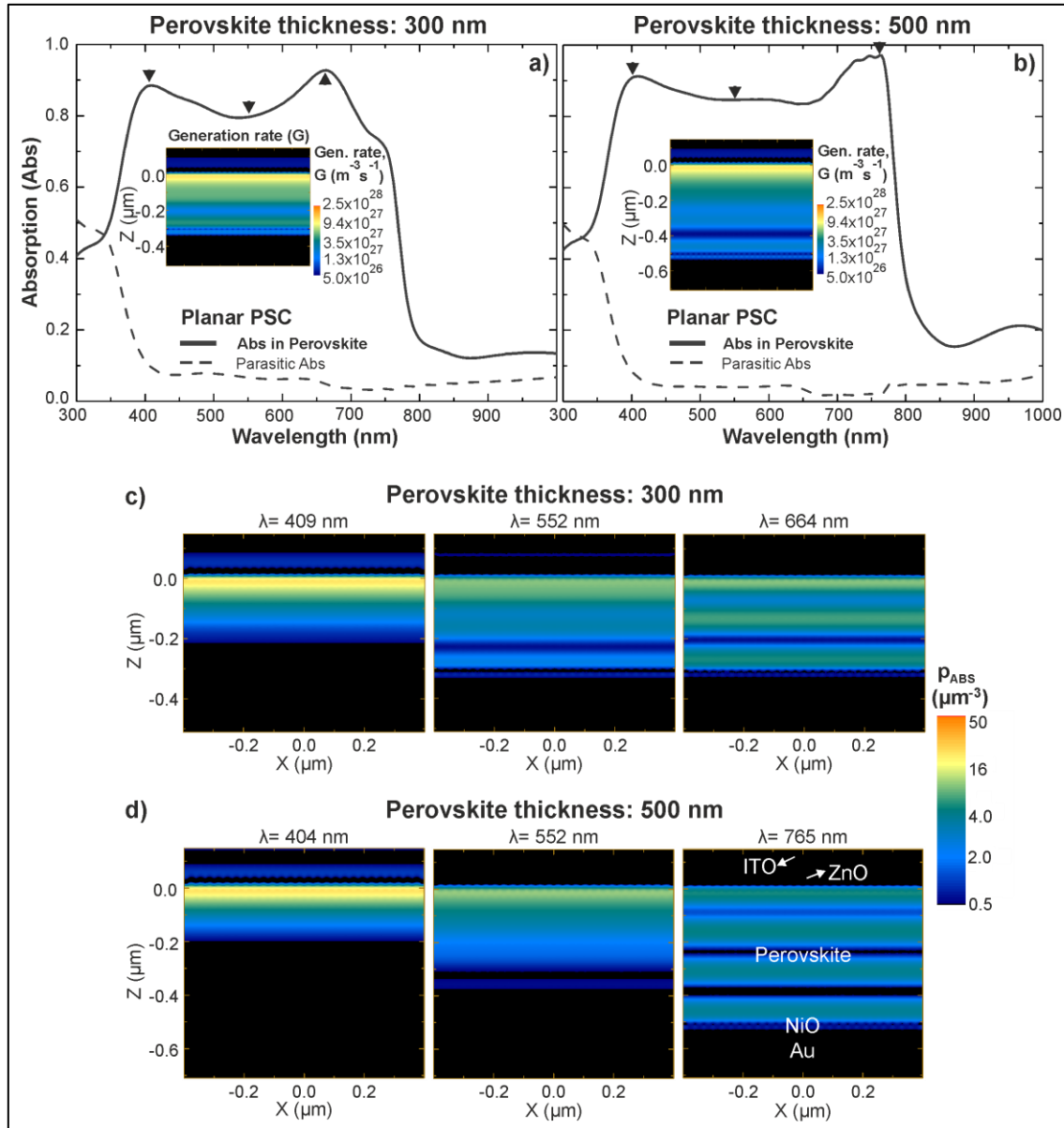


**Figure S4:** Contour plots of the calculated  $J_{\text{PH}}$  in PSCs with a planar substrate configuration, having either a 300 nm (a) or 500 nm (b) perovskite layer, as a function of the thicknesses of the front-located TCO ( $t_{\text{ITO}}$ ) and HTL ( $t_{\text{NiO}}$ ). The device layer structure is: flat substrate/metal electrode (200 nm Au)/HTL ( $\text{NiO}$ )/perovskite absorber/ETL (100 nm  $\text{ZnO}$ )/TCO (ITO), and light impinges from the cell side. The vertical and horizontal dashed lines mark the minimum  $t_{\text{ITO}}$  and  $t_{\text{NiO}}$  required to establish good-performing selective electron/hole contacts.

From Fig. S4 it is clear that the best  $t_{\text{ITO}}$  is close to zero, indicating that in this case the presence of the TCO is optically undesirable. This contracts with Fig. S2 simply because such TCO has a thicker underneath ETL (100 nm  $\text{ZnO}$ ) used in this substrate configuration (compared to the 25 nm  $\text{SnO}_2$  used as ETL in the superstrate configuration). Besides, the HTL is also optically unfavorable, since in both planar cases of Fig. S4 the best  $J_{\text{PH}}$  values generally occur for the lowest  $t_{\text{NiO}}$ . However, for their electrical purposes, minimum thicknesses ( $t_{\text{ITO}}=50$



nm and  $t_{\text{NiO}}=10$  nm) need to be guaranteed for these layers, so these were the values considered in the subsequent studies (marked by the dashed lines of Fig. S4 and indicated in row 4 of Table 1). However, it can be seen in the plots of Fig. S4 that other reasonable choices could also be made, for instance along the 50 nm-wide vertical stripe within about  $90 \text{ nm} < t_{\text{TO}} < 140 \text{ nm}$ , for both 300 and 500 nm perovskite.



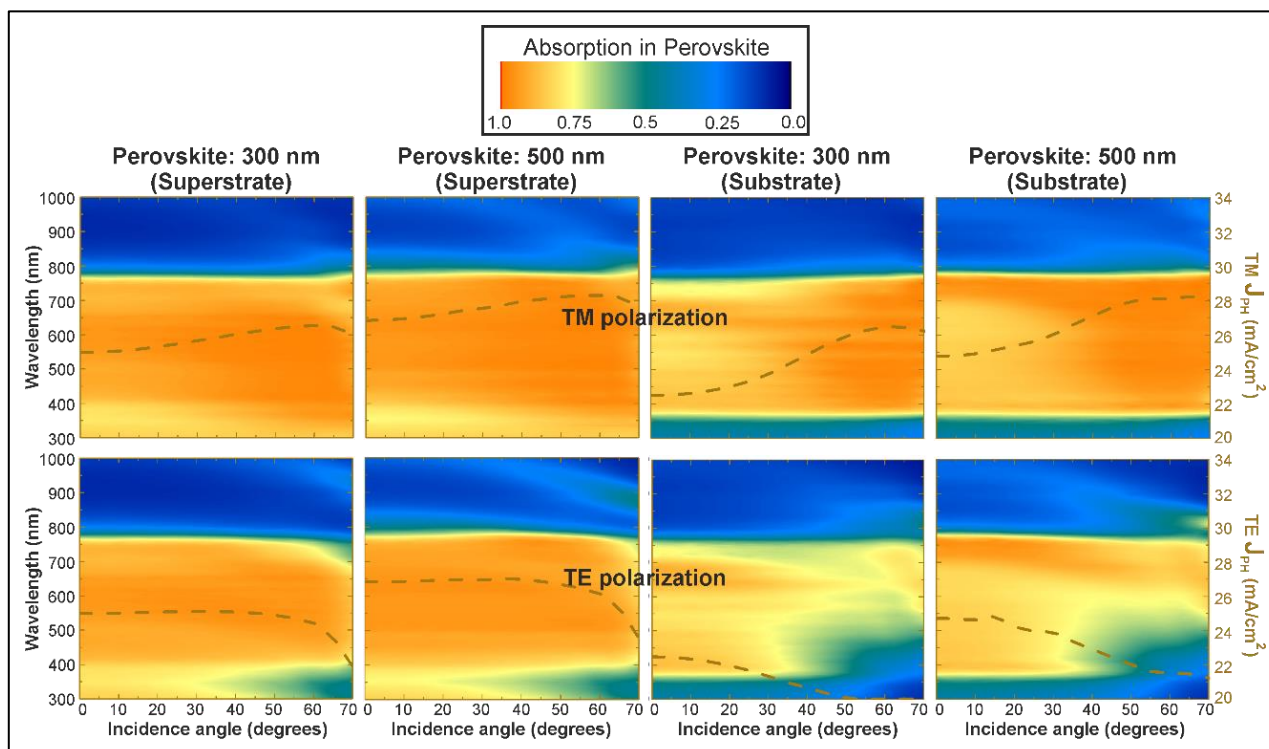
**Figure S5:** a,b) Spectra of the light absorption, attained with the selected TCO and HTL thicknesses and the fixed thickness of the ETL indicated in row 4 of Table 1, occurring in the perovskite absorber (solid lines) and the parasitic absorption in the other materials (dashed lines), considering perovskite films with distinct thickness: a) 300 nm and b) 500 nm in substrate configuration. The inset profiles show the log-scale distribution of the corresponding total generation rate,  $G$ , along the  $xz$  cross-sectional plane of the structures. c,d) Log-scale distributions of the absorption per unit volume ( $p_{\text{Abs}}$ ) along the same  $xz$  cross-sectional plane of the structures, at the wavelengths ( $\lambda$ ) of the absorption peaks marked by the black triangles in a) and b). The top surface of the perovskite layer is located at  $z=0$ .

Fig. S5a,b and Fig. S5c,d show the light absorption spectra and the absorption density profiles, respectively, attained with the planar PSCs in substrate configuration with the selected thicknesses of Table 1 (row 4). The absorption profiles of Fig. S5 and S2 present a similar overall behavior. However, the absolute  $J_{\text{PH}}$  is lower in substrate configuration, for both 300 and 500 nm perovskite (10% and 7%, respectively), compared to the superstrate configuration. This is mainly due to the thicker ETL ( $t_{\text{ZnO}}=100$  nm) used in this case, which parasitically absorbs more light in the 300-500 nm wavelengths, as seen in the spectra and inset  $G$  profiles of

Fig. S5a,b, as well as in the absorption density of Fig. S5c,d. Furthermore, ZnO has a lower refractive index value ( $n$ ) compared to SnO<sub>2</sub> and to ITO, thus providing worse index matching (reduced ARC effect) at the cell front when placed between the ITO and the perovskite.

### 7.4 Angle-resolved optical response of planar PSCs

The dependence of the photocurrent density of the planar PSCs with illumination direction is plotted in Fig. 4a,b for both cell configurations and absorber thicknesses. Fig. S6 presented here complements such information, showing how the absorption spectrum changes across the 0-70° angular range. Fig. 4a,b revealed a quite omnidirectional response of the planar PSCs, since these structures do not benefit from absorption gains in the longer wavelengths due to scattering effects which are more angular-sensitive. Fig. S6 shows that the absorption in the perovskite for the TM polarization even increases at certain large angles (>40°) for all cases. This is mainly attributed to Brewster-type effects which cause a drop in the reflection of the TM component and an increase in the reflection of the TE component, which also explains the reduction in the absorption of the TE component for large angles. However, the overall unpolarized  $J_{PH}$  (an average of TM and TE components) remains roughly constant along 0-60 degrees.



**Figure S6:** Contour plots of the absorption spectra occurring in the 300 and 500 nm perovskite absorber with planar PSCs in superstrate and substrate configurations, as a function of the incidence angle, for both TM (top) and TE (bottom) polarization. The dashed brown curve plotted in the contours corresponds to the angle-resolved photocurrent density obtained for each case (values in the right axes).

### 7.5 References

- [1] Refractive index database, (n.d.). <https://refractiveindex.info/> (accessed June 1, 2018).
- [2] J.-H. Kim, H.-J. Seok, H.-J. Seo, T.-Y. Seong, J.H. Heo, S.-H. Lim, K.-J. Ahn, H.-K. Kim, Flexible ITO films with atomically flat surfaces for high performance flexible perovskite solar cells, *Nanoscale*. 10 (2018) 20587–20598. doi:10.1039/C8NR06586A.
- [3] X. Wang, J. Wu, Y. Yang, X. Liu, Q. Guo, Z. Song, G. Li, Z. Lan, M. Huang, High performance and stable perovskite solar cells using vanadic oxide as a dopant for spiro-OMeTAD, *J. Mater. Chem. A*. 7 (2019) 13256–13264. doi:10.1039/C9TA03351C.



- [4] K.-H. Jung, J.-Y. Seo, S. Lee, H. Shin, N.-G. Park, Solution-processed SnO<sub>2</sub> thin film for a hysteresis-free planar perovskite solar cell with a power conversion efficiency of 19.2%, J. Mater. Chem. A. 5 (2017) 24790–24803. doi:10.1039/C7TA08040A.